

# WALLABY Pre-Pilot and Pilot Survey: the Tully Fisher Relation in Eridanus, Hydra, Norma and NGC4636 fields

Hélène M. Courtois<sup>1\*</sup>, Khaled Said<sup>2</sup>, Jeremy Mould<sup>3</sup>, T.H. Jarrett<sup>4</sup>, Daniel Pomarède<sup>5</sup>, Tobias Westmeier<sup>6,7</sup>, Lister Staveley-Smith<sup>6,7</sup>, Alexandra Dupuy<sup>1,22</sup>, Tao Hong<sup>8</sup>, Daniel Guinet<sup>1</sup>, Cullan Howlett<sup>2</sup>, Nathan Deg<sup>9</sup>, Bi-Qing For<sup>6</sup>, Dane Kleiner<sup>10</sup>, Bärbel Koribalski<sup>11,12</sup>, Karen Lee-Waddell<sup>6,15</sup>, Jonghwan Rhee<sup>6,7</sup>, Kristine Spekkens<sup>13</sup>, Jing Wang<sup>14</sup>, O.I. Wong<sup>15,6,7</sup>, Frank Bigiel<sup>16</sup>, Albert Bosma<sup>17</sup>, Matthew Colless<sup>18</sup>, Tamara Davis<sup>2</sup>, Benne Holwerda<sup>19</sup>, Igor Karachentsev<sup>20</sup>, Renée C. Kraan-Korteweg<sup>4</sup>, Kristen B.W. McQuinn<sup>21</sup>, Gerhardt Meurer<sup>6</sup>, Danail Obreschkow<sup>6,7</sup>, Edward Taylor<sup>3</sup>

<sup>1</sup>University Lyon 1, IUF, IP2I Lyon, 69622 Villeurbanne cedex, France

<sup>2</sup>School of Mathematics and Physics, The University of Queensland, Brisbane, QLD 4072, Australia

<sup>3</sup>Centre for Astrophysics & Supercomputing, Swinburne University, Australia

<sup>4</sup>Astronomy Department, University of Cape Town, Private Bag X3, Rondebosch, 7701, South Africa

<sup>5</sup>IRFU, CEA Université Paris-Saclay, 91191 Gif-sur-Yvette, France

<sup>6</sup>International Centre for Radio Astronomy Research (ICRAR), The University of Western Australia, M468, Crawley, WA 6009, Australia

<sup>7</sup>ARC Centre of Excellence for Astrophysics in 3 Dimensions (ASTRO 3D), Australia

<sup>8</sup>National Astronomical Observatories, Chinese Academy of Sciences, 20A Datun Road, Chaoyang District, Beijing 100012, China

<sup>9</sup>Department of Physics, Engineering Physics and Astronomy Queen's University Kingston, ON K7L 3N6, Canada

<sup>10</sup>INAF - Osservatorio Astronomico di Cagliari, Via della Scienza 5, 09047 Selargius, CA, Italy

<sup>11</sup>Australia Telescope National Facility, CSIRO Astronomy and Space Science, P.O. Box 76, NSW 1710, Epping, Australia

<sup>12</sup>Western Sydney University, Locked Bag 1797, Penrith, NSW 2751, Australia

<sup>13</sup>Royal Military College of Canada, PO Box 17000, Station Forces, Kingston, Ontario, Canada K7K7B4

<sup>14</sup>Kavli Institute for Astronomy and Astrophysics, Peking University, Beijing 100871, China

<sup>15</sup>CSIRO Space & Astronomy, PO Box 1130, Bentley, WA 6102, Australia

<sup>16</sup>Argelander-Institut für Astronomie, Universität Bonn, Auf dem Hügel 71, 53121 Bonn, Germany

<sup>17</sup>Aix Marseille Univ, CNRS, CNES, LAM, Marseille, France

<sup>18</sup>Research School of Astronomy and Astrophysics, Australian National University, Canberra, ACT 2611, Australia

<sup>19</sup>University of Louisville, Department of Physics and Astronomy, 102 Natural Science Building, 40292 KY Louisville, USA

<sup>20</sup>Special Astrophysical Observatory, Russian Academy of Sciences, Russia

<sup>21</sup>Rutgers University, Department of Physics and Astronomy, 136 Frelinghuysen Road, Piscataway, NJ 08854, USA

<sup>22</sup>Korea Institute for Advanced Study, 85, Hoegi-ro, Dongdaemun-gu, Seoul 02455, Republic of Korea

Accepted October 19th 2022 for MNRAS

## ABSTRACT

The WALLABY pilot survey has been conducted using the Australian SKA Pathfinder (ASKAP). The integrated 21-cm HI line spectra are formed in a very different manner compared to usual single-dish spectra Tully-Fisher measurements. It is thus extremely important to ensure that slight differences (e.g. biases due to missing flux) are quantified and understood in order to maximise the use of the large amount of data becoming available soon. This article is based on four fields for which the data are scientifically interesting by themselves. The pilot data discussed here consist of 614 galaxy spectra at a rest wavelength of 21cm. Of these spectra, 472 are of high enough quality to be used to potentially derive distances using the Tully-Fisher relation. We further restrict the sample to the 251 galaxies whose inclination is sufficiently close to edge-on. For these, we derive Tully-Fisher distances using the deprojected WALLABY velocity widths combined with infrared (WISE W1) magnitudes. The resulting Tully-Fisher distances for the Eridanus, Hydra, Norma and NGC 4636 clusters are 21.5, 53.5, 69.4 and 23.0 Mpc respectively, with uncertainties of 5–10%, which are better or equivalent to the ones obtained in studies using data obtained with giant single dish telescopes. The pilot survey data show the benefits of WALLABY over previous giant single-dish telescope surveys. WALLABY is expected to detect around half a million galaxies with a mean redshift of  $z = 0.05(200\text{Mpc})$ . This study suggests that about 200,000 Tully-Fisher distances might result from the survey.

**Key words:** surveys – radio astronomy: 21 cm – galaxies: distances and redshifts – cosmology: large-scale structure of Universe

\* E-mail: helene.courtois@univ-lyon1.fr

## 1 INTRODUCTION

Tully & Fisher (1977) discovered a relation (the Tully-Fisher relation: TFR) between the extensive properties of disk galaxies (mass, luminosity, and radius) and their rotation velocity, which can be derived from the velocity width of their neutral hydrogen 21 cm spectra. If galaxy surface brightness, stellar mass, and mass to light ratio are functions of halo mass, the virial theorem leads one to expect a luminosity – rotation velocity relation. As the TFR relates distance-independent and distance-dependent quantities, it can be used to measure galaxy distances and peculiar velocities. Developments in understanding galaxy scaling relations are reviewed by Mould (2020). The TFR is also reproduced in dark matter simulations, when sub-grid physics is added to follow the baryons (e.g. Springel et al. 2018), so it can therefore also be used to further probe the astrophysics of galaxy formation.

The Widefield ASKAP L-band Legacy All-sky Blind Survey (WALLABY) pre-pilot and pilot phase 1 survey is an observational study of four fields with the Australian Square Kilometer Array Pathfinder (ASKAP) telescope. The pilot observations are a precursor to the full WALLABY survey, a blind neutral hydrogen survey of the Southern hemisphere (Koribalski et al. 2020) which is scheduled to begin in 2022. The pilot data has already been used to study HI content of galaxies in groups (For et al. 2021), discover dark clouds in the vicinity of galaxies (Wong et al. 2021), and study the diversity of ram pressure stripping of HI gas in galaxies in the Hydra cluster (Wang et al. 2021).

The raw ASKAP visibilities from the WALLABY observations are processed and reduced using ASKAPsoft. The processed data products are available on CASDA. The data are first released to the WALLABY team for analysis, and, once published, available to the wider community. A mosaic of individual footprints is then made to produce the final full sensitivity cubes which are run through the SoFiA pipeline. SoFiA is a 3D source finding and parametrisation software package (Serra et al. 2015; Westmeier et al. 2021) which, amongst many other outputs, produces a 1-dimensional spectrum by spatially integrating all emission within its mask. The measured HI linewidth is a measure of the galaxy projected rotation velocity.

In this article we explore the infrared TFR, by combining WALLABY pilot HI spectra with photometric data using WISE W1 band infrared fluxes. Infrared wavelengths have the advantage of markedly lower extinction of galaxy radiation by dust (Aaronsen et al. 1979). It is now well known that using infrared data provides a tighter TFR than using optical bands (Sorice et al. 2013; Neill et al. 2014; Kourkchi et al. 2020b). The measured galaxy distances can be used to: measure the expansion rate through determination of the Hubble constant (Kourkchi et al. 2020b); test the  $\Lambda$ CDM cosmological model using measurements of the bulk flow (Hoffman et al. 2015; Hong et al. 2019); compute systematics in the SNIa Hubble constant determination (Peterson et al. 2021). Another question that measurements of non-Hubble flows can address is the quantity of matter needed in specific regions such as the Great Attractor in order to explain gravitationally-induced motions, with the aim of reconciling with observed baryonic matter distribution (Said et al. 2020; Thévenot et al. 2020).

A major benefit of the WALLABY survey is its higher sensitivity compared to previous southern surveys used for Tully-Fisher distances – for example, the HI Parkes All-Sky Survey (HIPASS) (Koribalski et al. 2004; Meyer et al. 2004). It also has higher survey speed than northern single-dish telescopes previously used to conduct HI surveys (Haynes et al. 2018) thanks to its wide (30 sq.deg) instantaneous field of view, thus enabling to construct larger galaxy

**Table 1.** Table of J2000 coordinates pointings of the WALLABY pre-pilot and pilot phase 1 survey fields.

Footprint	Field centre (J2000)	
	RA	DEC
Eridanus A	03:39:30.000	-22:23:00.00
Eridanus B	03:36:44.520	-22:37:54.69
Hydra-1A	10:15:47.844	-27:22:27.66
Hydra-1B	10:17:49.958	-27:49:24.30
Hydra-2A	10:39:24.238	-27:22:27.66
Hydra-2B	10:41:26.352	-27:49:24.30
NGC4636-1A	12:38:02.328	-00:26:59.95
NGC4636-1B	12:39:50.337	-00:53:59.85
NGC4636-2A	12:38:02.729	+04:56:58.64
NGC4636-2B	12:39:51.059	+04:29:58.13
Norma-1A	16:16:30.928	-59:27:41.88
Norma-1B	16:20:06.332	-59:54:30.90
Norma-2A	16:55:26.063	-59:27:41.88
Norma-2B	16:59:01.467	-59:54:30.90

samples. Other advantages are the location of ASKAP at a site that is free from terrestrial radio frequency interference and its high angular resolution, which allows detailed morphological and dynamical studies. Although angular resolution is not important for this TFR study, it does lessen the probability of beam confusion and will allow future dynamical measurements of inclination.

All-sky infrared surveys provide complementary data for large samples of galaxies with a depth, resolution and photometric accuracy suitable for TFR studies. Examples include the 2MASS Tully-Fisher (2MTF) survey of 2,062 galaxies (Hong et al. 2019) and the WISE Tully-Fisher study of Lagattuta et al. (2013). Currently, the largest Tully-Fisher samples are of the order of 10,000 galaxies (Kourkchi et al. 2020b), while WALLABY is planned to triple or more this latter number in the next few years (Koribalski et al. 2020). The Meerkat SKA precursor located in South Africa is also used to successfully derive baryonic Tully-Fisher galaxy distances (Ponomareva et al. 2021).

Galaxy distances are key to the objective of the CosmicFlows (CF) project (Tully et al. 2016), which is to improve the cosmography of the nearby universe including the location and mass measurement of the largest attractors. Distances are used to compute velocity deviations from the Hubble cosmic expansion which are assumed to arise from the large-scale gravitational field. This can only be realized with very accurate distances. The CF project started in 2006 and will shortly publish its fourth generation catalogue containing about 45,000 accurate determinations of galaxy distances.

In this paper we describe the pre-pilot and phase 1 pilot WALLABY surveys from which our HI data is drawn, and present optical identifications of the detected sourced at 21 cm (§2); we form TFRs by using accurate photometry in the WISE W1 bandpass (§3). Finally, we show how the WALLABY Survey can add to the CF database for future studies of large-scale structure.

## 2 WALLABY PRE-PILOT AND PILOT SURVEY

WALLABY is an extragalactic all-sky HI survey with the ASKAP telescope which consists of  $36 \times 12$  m dishes with baselines ranging from 22 m to 6 km (Hotan et al. 2021). It is equipped with phased array feeds with a field-of-view of about 30 deg<sup>2</sup> at 1.4 GHz. The frequency coverage of ASKAP is from 0.7 to 1.8 GHz with an in-

stantaneous bandwidth of 288 MHz. Its spectral resolution of 18.5 kHz translates into a velocity resolution of  $4 \text{ km s}^{-1}$  at redshift zero.

For the WALLABY pilot surveys, a bandwidth of 144 MHz covering the frequency range of 1295.5 to 1439.5 MHz, was processed and imaged. This corresponds to redshifts  $z < 0.096$ . All baselines, including the 6 km baselines, were calibrated. However, the current WALLABY images only include baselines up to 2 km, resulting in an angular resolution of  $30''$ . The nominal RMS noise level is approximately 1.6 mJy after 2 footprints, each of duration 8 h, are combined. We refer the reader to [Koribalski et al. \(2020\)](#) for more details about the WALLABY survey.

## 2.1 Radio and photometry data measurements

The pre-pilot and pilot phase 1 survey resulted in coverage of the NGC4636 group, the Eridanus super-group, the Hydra I cluster, and the Norma cluster surrounds (the actual Norma cluster is excluded from this study due to strong residual radio continuum emission). Sources were catalogued using the SoFIA source finding pipeline ([Serra et al. 2015](#); [Westmeier et al. 2021](#)). Detections were linked across a spatial and spectral radius of 2 pixels with a minimum size requirement for reliable source identification of 5 spatial pixels and 8 spectral channels. SoFIA's reliability filter was then applied to remove all detections with a reliability below 0.8, using a Gaussian kernel density estimator of size 0.35 times the covariance. All remaining sources were then parameterised, assuming a restoring beam size of  $30''$  for all integrated flux measurements. The source detection details slightly vary between the four different fields – details will be provided in the upcoming paper accompanying the first public data release of phase 1 pilot data ([Westmeier et al. in prep. 2022](#)).

The pre-pilot field containing the Eridanus super group was observed with two interleaving footprints (A and B) with an offset of  $38'$ , and rotated by a position angle of  $45 \text{ deg}$  relative to a standard ASKAP footprint. The Norma, Hydra and NGC4636 pilot observations were of two adjacent  $30 \text{ sq.deg}$  overlapping tiles (1 and 2) with the tile centres separated by  $5.4 \text{ deg}$ . Each tile consisted of two slightly offset footprints observed for 8 hours. Therefore, each 1-D HI spectrum has an effective integration time of 16 hr. The centres of the footprints are given in Table 1.

## 2.2 Comparison of velocity width measurement algorithms

SoFIA provides approximate linewidths for all galaxies that it finds in WALLABY cubes. However, to improve robustness, accuracy, reliability and compatibility with previous measurements, we also compute linewidths using the CF methodology and make a detailed comparison with the SoFIA estimates. The CF linewidth  $W_{m50}$ , is measured at the flux level that is 50% of the mean flux, averaged in channels within the wavelength range enclosing 90% of the total integrated flux ([Courtois et al. 2011a,b](#)). It is followed by a correction for redshift and instrumental broadening:  $W_{m50}^{\text{corr}} = (W_{m50} - 2\Delta\nu\lambda)/(1+z)$ , where  $z$  is the redshift in the CMB frame,  $\Delta\nu$  is the smoothed spectral resolution, and  $\lambda = 0.25$  is an empirically determined constant ([Courtois et al. 2009](#)). The observed line width was also adjusted by separating out the broadening from turbulent motions and offsets to produce an approximation to  $2V_{\text{max}}$ , where  $V_{\text{max}} = W_{m50}/2$  correspond to the rotation rate over the

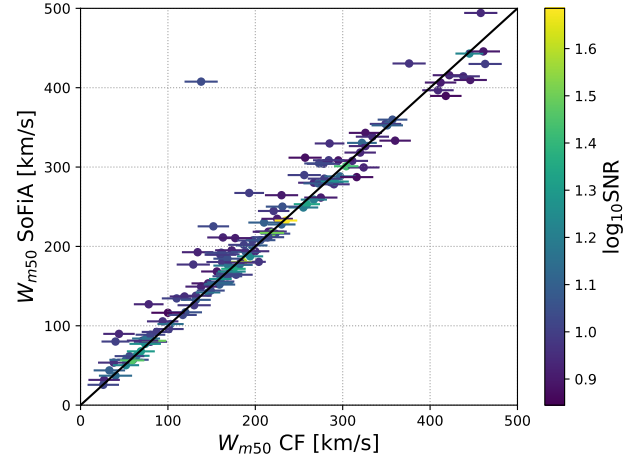


**Figure 1.** Linewidths  $W_{m50}$  in the Norma field as measured by the CosmicFlows (CF) algorithm compared with the automatic measurements of SoFIA, colour-coded by S/N ratio. The plot only includes spectra with an error on  $W_{m50}$  less or equal to  $20 \text{ km s}^{-1}$ . Two further spectra with low S/N ratio, where the linewidth difference exceeds  $100 \text{ km s}^{-1}$ , are excluded from the plot.

main body of a galaxy. [Tully & Fouqué \(1985\)](#) define the parameter  $W_{\text{mx}}$  as:

$$W_{\text{mx}}^2 = W_{m50}^{\text{corr},2} + W_{t,m50}^2 \left[ 1 - 2e^{-(W_{m50}^{\text{corr}}/W_{c,m50})^2} - 2W_{m50}^{\text{corr}}W_{t,m50} \left[ 1 - e^{-(W_{m50}^{\text{corr}}/W_{c,m50})^2} \right] \right]. \quad (1)$$

The parameters  $W_{c,m50} = 100 \text{ km s}^{-1}$  and  $W_{t,m50} = 9 \text{ km s}^{-1}$  are set following tests conducted in [Courtois et al. \(2009\)](#), and characterize respectively the transition from boxcar to Gaussian intrinsic profiles, and the turbulent broadening for the observed linewidth considered. It is then related to the rotation rate  $V_{\text{max}}$  by:

$$V_{\text{max}} = \frac{W_{\text{mx}}}{2 \sin(i)}, \quad (2)$$

where  $i$  is the inclination of the galaxy from face-on relative to the observer.

Details regarding the  $W_{m50}$  and  $W_{\text{mx}}$  line width parameters and comparisons with alternatives are discussed in [Courtois et al. \(2009\)](#). A comparison of the CF and SoFIA linewidth measurements in the Norma field is shown in Fig. 1.

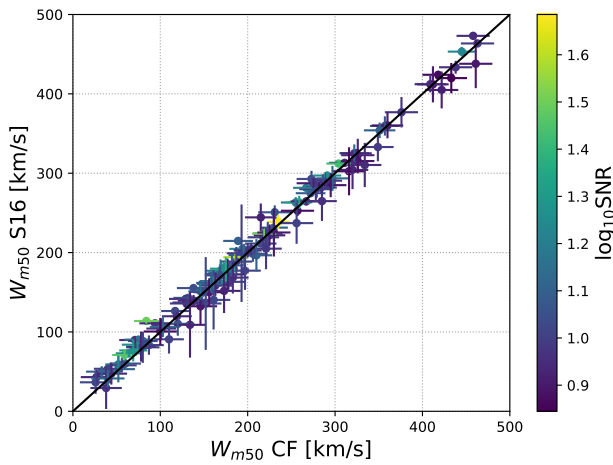
We make a further comparison with velocity widths derived using the method described by [Said et al. \(2016\)](#) (hereafter S16). This algorithm requires prior knowledge of the left and right horns which is currently done manually and returns the linewidth measured at 50% of the mean flux and its associated uncertainty. In this paper, we compare the CF linewidth with the S16 linewidth measured at 50% of the mean flux, as shown in Fig. 2.

We use the relative error between pairs of measurements to quantitatively check for any large discrepancies between 50% widths measured with the CF algorithm and widths measured at 50% of the mean flux with the S16 algorithm. We used the pairwise relative error of the form:

$$\varepsilon = \frac{W_{m50}^{\text{CF}} - W_{m50}^{\text{S16}}}{\sqrt{(eW_{m50}^{\text{CF}})^2 + (eW_{m50}^{\text{S16}})^2}}, \quad (3)$$

**Table 2.** All galaxies with pairwise relative error  $|\epsilon| > 1.0$  between the CosmicFlows and S16 algorithms.

name	PGC	$W_{m50}$	$eW_{m50}$	$W_{m50}^{S16}$	$e_{W_{m50}}^{S16}$	$\epsilon$
J102439-244547	30532	94	18	112	2	-1.0177
J102447-264054	30545	271	17	322	13	-2.4078
J103442-283406	31296	247	15	263	4	-1.0149
J103726-261843	31557	199	18	224	2	-1.3854
J104127-275119	31842	99	19	119	5	-1.0091
J104142-284653	31855	107	15	128	7	-1.2566
J104513-262755		50	17	74	6	-1.3571
J104905-292232	32361	117	17	142	3	-1.4259
J163452-603705	58536	189	17	215	1	-1.5087
J164359-600237		215	18	244	17	-1.1702
J165105-585918	59112	84	14	114	3	-2.0721
J165145-590915		71	18	90	5	-1.0111

**Figure 2.** Comparison of 50% linewidths in the Norma field measured with the CF algorithm and linewidths measured at 50% of the mean flux using the S16 algorithm (Said et al. 2016). Only measurements of spectra with an adequate quality are displayed (error on  $W_{m50}$  less or equal to  $20 \text{ km s}^{-1}$ ). This comparison displays a typical scatter at  $20 \text{ km s}^{-1}$ .

where  $W_{m50}^{CF}$ ,  $W_{m50}^{S16}$ ,  $eW_{m50}^{CF}$ , and  $eW_{m50}^{S16}$  are the 50% widths measurements from CosmicFlows and S16 algorithms and their associated statistical uncertainties, respectively. Values of  $\epsilon$  for all galaxies are within the distribution of a Gaussian with a mean of zero and a standard deviation of unity. Table 2 lists all discrepant measurements with  $|\epsilon| > 1.0$ .

Following the CosmicFlows collaboration, the signal-to-noise ratio is calculated by taking the mean flux density across all channels in excess of 95% of the peak and dividing it by the noise level in the spectrum as measured outside of the HI line (Courtois & Tully 2015).

The error on the linewidth  $e_W$  in  $\text{km s}^{-1}$ , follows the empirical relation from (Courtois et al. 2009):

$$\begin{aligned}
 \text{SNR} \geq 17 & \quad e_W = 8 \text{ km s}^{-1}; \\
 2 < \text{SNR} < 17 & \quad e_W = 21.6 - 0.8 \times \text{SNR} \text{ km s}^{-1}; \\
 \text{SNR} \leq 2 & \quad e_W = 70 - 25 \times \text{SNR} \text{ km s}^{-1},
 \end{aligned} \tag{4}$$

where SNR is the signal-to-noise ratio. CosmicFlows has shown that an HI spectrum is considered adequate for estimating galaxy distance

through the TFR if the error on  $W_{m50}$  is less or equal to  $20 \text{ km s}^{-1}$ . As seen in Fig. 2 this threshold is confirmed once again by this study.

In summary for the three algorithms for  $W_{m50}$ : (1) SoFiA is automated but sometimes gives discrepant measurements for low SNR spectra (see Fig. 1). It also has a dispersion of about  $50 \text{ km s}^{-1}$ , which is too high for Tully-Fisher purposes (Courtois et al. 2009). (2) The adopted CF algorithm is semi-automated, with a final inspection by eye of the fit. In some cases (six spectra, corresponding to about 1% of all spectra in the pilot survey), a fit was not possible. (3) The S16 algorithm requires a starting value for  $W_{m50}$  (that can be provided by SoFiA), but appears to provide a measurement which is within the  $20 \text{ km s}^{-1}$  error limit on  $W_{m50}$  that we impose for TFR studies. Therefore the WALLABY survey data will be treated by all three algorithms. The comparison of the results per individual galaxy will allow to identify the difficult spectra that require close inspection.

Details of all the galaxies selected at 21 cm for this TF study are listed in Appendix A.

### 2.3 Comparison with previous single-dish velocity width measurements

In this section we check whether there are any differences between single-dish and multi-dish spectroscopic data, that would affect the quality of the derived Tully-Fisher distances with systematic errors.

Fortunately, there is a sufficient overlap with existing data to check consistency between pilot WALLABY and published single-dish velocity widths as compiled in the Extragalactic Distance Database (Courtois & Tully 2015). This comparison is shown in Fig. 3 for the galaxies in common. There is no significant difference when comparing the WALLABY  $W_{mx}$  values with those measured from single-dish data, with most agreeing within the  $20 \text{ km s}^{-1}$  limit. The discrepant data comes from wrong width measurements from low S/N ratio Arecibo spectra and measurements of WALLABY spectra containing residual continuum from strong nearby sources outside the field and therefore not cleaned. This comparison is an excellent external robustness assessment of the capability of WALLABY to deliver satisfactory HI data to the community. It also demonstrates that the exposure time used for the Phase 1 Pilot Survey can be considered as the guideline for the upcoming large WALLABY survey.

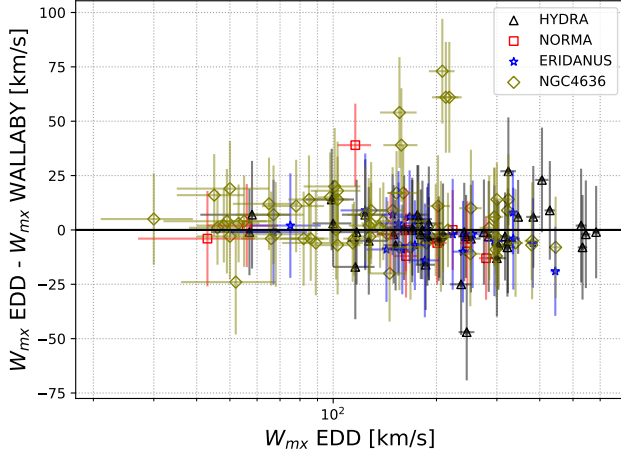


**Figure 3.** Comparison of the WALLABY pilot phase velocity widths presented in this article with single-dish data in the Extragalactic Distance Database (Courtois & Tully 2015). Widths are only compared where the internal error for  $W_{m50}$  in both datasets is less or equal to  $20 \text{ km s}^{-1}$ . Measurements mostly agree within the  $20 \text{ km s}^{-1}$  limit. The large offsets are either due to low SNR Arecibo spectra or due to noisy WALLABY spectra with residual baseline ripples due to residuals caused by strong radio continuum sources. The latter is more prominent in the NGC4636 field, which lies close to 3C273.

## 2.4 WISE photometry

The *Wide-Field Survey Explorer* (WISE) satellite provides all-sky photometric observations in 4 mid-infrared bands,  $W1 = 3.4\mu\text{m}$ ,  $W2 = 4.6\mu\text{m}$ ,  $W3 = 12.0\mu\text{m}$ ,  $W4 = 22.8\mu\text{m}$  (Wright et al. 2010).

We initially tried to use data from the WISE all sky catalog GATOR web interface. When plotting the TFR we found that this instrumental profile-fit magnitudes were not appropriate for photometry of extended sources. As can be seen in Fig. 4, the derived Tully-Fisher relation was totally unprobable.

Thus for this analysis, the photometric parameters are measured from the WISE observations using the photometric pipeline from Jarrett et al. (2013), where mosaics of each source are optimally constructed for resolved sources, carefully preserving the native angular resolution of WISE single frames (Jarrett et al. 2012). Source characterization includes size, shape, orientation, surface brightness and photometric measurements.

These measurements serve as the basis for derived physical parameters, including size, luminosity, stellar mass and star formation rate. The aggregate stellar mass is estimated using the  $W1$  in-band luminosity and the  $W1$ - $W2$  colour (to account for the population-dependent mass-to-light ratio), as described in Cluver et al. (2014). The global star formation rate is estimated from the  $W3$  and  $W4$  spectral luminosities, after subtracting the stellar continuum, as detailed in Cluver et al. (2017); Jarrett et al. (2019).

The pipeline returns several types of apparent magnitude including, 1-sigma isophotal magnitudes, asymptotic magnitudes, and total radial-profile-modeled magnitudes. The Tully-Fisher relation is an empirical relation between maximum rotation velocity and total luminosity, i.e total stellar mass) of the galaxy. We therefore used the total extrapolated magnitude which encompasses the isophotal measured magnitude plus extrapolation of the radial SB profile to 3 disk scale lengths for our analysis.

The second measured parameter that is needed for the TFR is the

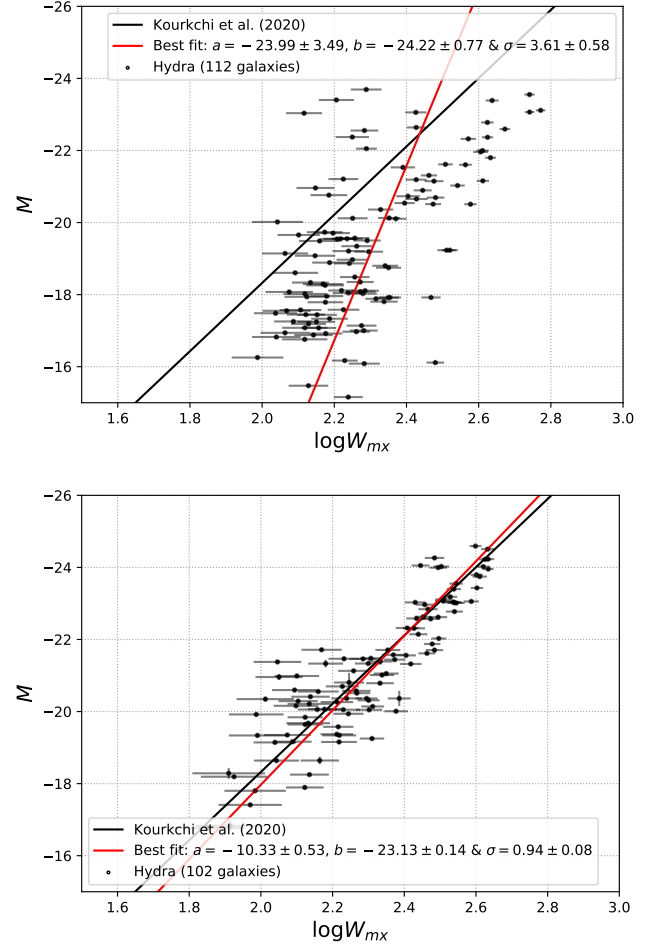


**Figure 4.** Comparison of TFR for Hydra using the public WISE photometry (top-panel) and using our newly derived WISE photometry. The rms deviations from the best fit line (red-line) decreases from 3.6 to 0.9 when using the new photometry. Furthermore, the best fit parameters are very close to the universal calibrated relation. The best fit parameters (red lines) are from the hyperfit package (Robotham & Obreschkow 2015) which uses errors in both axes.

inclination which is extracted from the WISE observations. We used the measured axis ratio based on the  $W1$  3-sigma isophote to derive the inclination. We caution that the axis ratio and position angle are sensitive to the angular size of the galaxy due to the relatively large beam,  $\text{FWHM} = 6''$ , of the  $W1$  imaging. Moreover, the near-infrared is sensitive to older stellar populations, and notably the bulge population, which tends to circularize the axis ratio and hence appear more face-on with inclination.

## 3 TULLY-FISHER DISTANCES

Measuring distances requires a redshift independent distance indicator which can be either a primary indicator such as the Cepheid variable stars (Ferne 1969) or a secondary indicator such as, the Tully-Fisher relation (Tully & Fisher 1977). In this paper, we will be adopting the Tully-Fisher relation as our workhorse to measure distances to spiral galaxies in the four WALLABY fields. As the name suggests, a secondary distance indicator such as the TFR should be

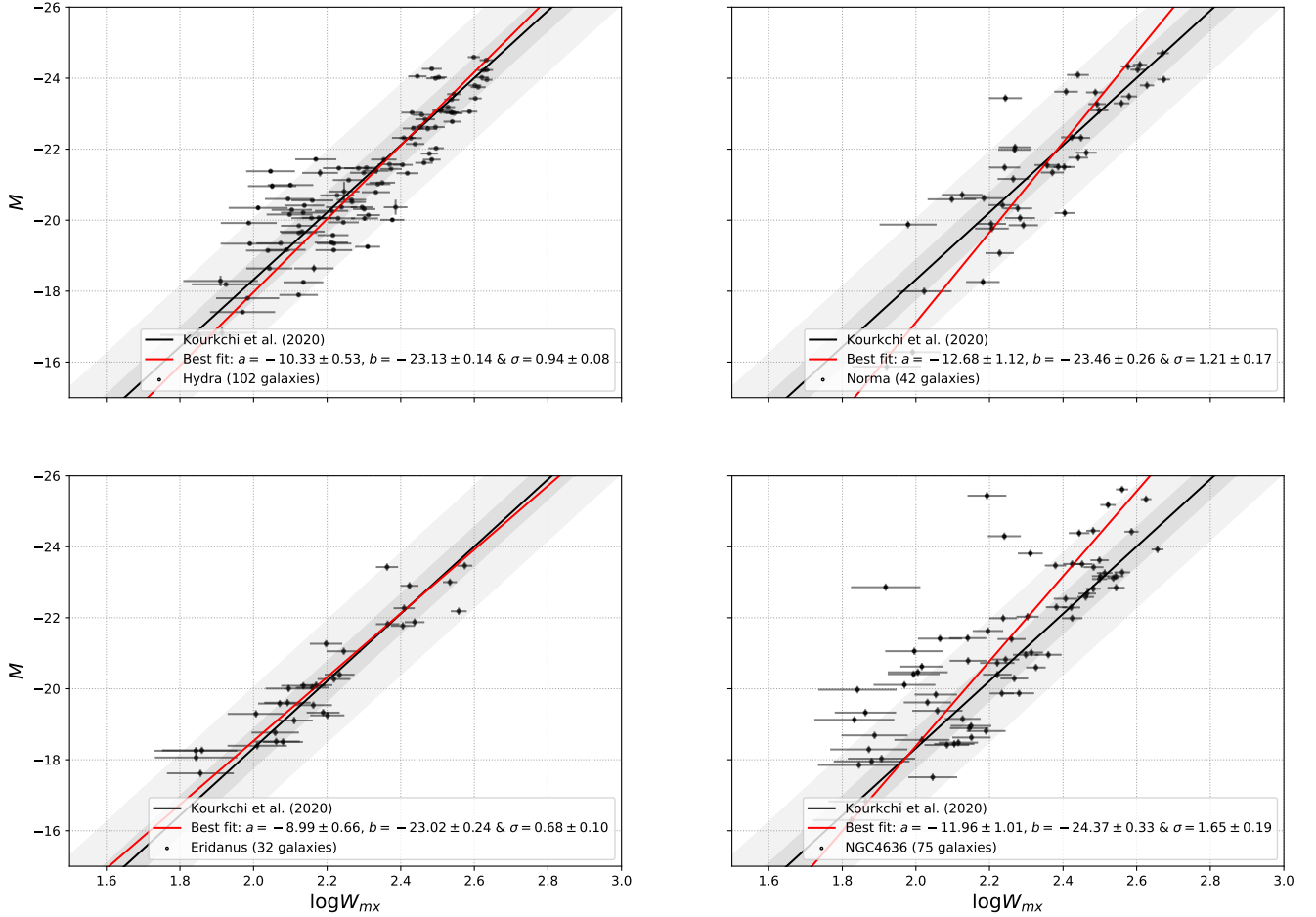


**Figure 5.** TFR for the four fields in the WISE *W1* band. The solid black line is the calibrated TFR from [Kourkchi et al. \(2020a\)](#); the dark and light shaded areas correspond to  $1\text{-}\sigma$  and  $3\text{-}\sigma$  scatter around the TFR, respectively; the solid red line is the best fit model. The quantities derived with the Pilot survey are in good agreement with the WISE *W1* TFR calibration in K20 in the Hydra, Norma and Eridanus fields. The high scatter in the NGC4636 field is due to the noisy spectra caused by residual radio continuum.

calibrated first using a sample of spiral galaxies with known distances.

[Kourkchi et al. \(2020a, K20 hereafter\)](#) re-calibrated the TFR using optical *u*, *g*, *r*, *i* and *z* SDSS bands as well as infrared *W1* and *W2* WISE bands. In this article, we will use their WISE *W1* calibrated relation as our standard tool in deriving the distances of galaxies in the WALLABY fields with, as plotted in Fig. 4 and Fig. 5, a slope of  $-9.47 \pm 0.14$ , a zero point of  $-20.36 \pm 0.07$  and rms of 0.58. Although the sample used to re-calibrated the TF is different from our WALLABY sample, parameters, methods and corrections should be as consistent as possible. In this section we will go through all parameters that we used to derive the distances for all four WALLABY fields and their associated corrections.

With the calibrated TFR in WISE *W1* (K20) in hand, two sets of observations are required to derive TF distances: (A) spectroscopic observations (in our case HI 21-cm) from which we extract the galaxy rotational velocity; (B) photometric observations (in our case infrared imaging) from which we extract the apparent magnitude for each galaxy in our sample.

The first set of data is the WALLABY 21-cm spectra. The raw spectra were fitted using three different algorithms. The full pre-

sentation of this data set is in Section 2. To be consistent with the calibrated TFR from K20, we used the same method and corrections as CosmicFlows to derive the  $W_{\text{mx}}$  line width (i.e., see section 2.2). The only difference is that, while CosmicFlows visually measured inclinations, here we are using WISE *W1* band photometric parameters (Section 2.4) to derive the inclination as:

$$\cos^2 i = \frac{(b/a)^2 - q_0^2}{1 - q_0^2} \quad (5)$$

where  $q_0$  is the intrinsic axial ratio of the galaxy,  $q_0 = 0.13$  for Sbc and Sc, and  $q_0 = 0.2$  for other types ([Giovanelli et al. 1997](#)). We didn't make a search for the morphological type, so we used  $q_0 = 0.2$  if  $b/a > 0.2$  and  $q_0 = 0.13$  if  $b/a \leq 0.2$ . Galaxies with axial ratio ( $b/a$ ) greater or equal to 0.7 are excluded to avoid large corrections in the line width due to the inclination correction.

The heliocentric redshift can be measured from the WALLABY 21-cm spectra. We use redshifts to visualize the data (e.g., Fig. 5 and

8). For the purpose of this paper, we first convert the heliocentric redshift  $z_{\text{helio}}$  to the CMB redshift  $z_{\text{CMB}}$  using,

$$z_{\text{CMB}} = \frac{1 + z_{\text{helio}}}{1 + z_{\text{Sun}}} - 1, \quad (6)$$

where  $z_{\text{Sun}}$  is the velocity of the sun with respect to the CMB in the direction of the galaxy being measured. It is calculated using the Planck dipole (Planck Collaboration et al. 2020). We derive the comoving distance  $D(z_{\text{CMB}})$  in Mpc at redshift  $z_{\text{CMB}}$  using a flat  $\Lambda$ CDM with  $H_0 = 75 \text{ km s}^{-1} \text{ Mpc}^{-1}$  and  $\Omega_m = 0.27$  and convert this to luminosity distances using:

$$D_L = (1 + z_{\text{helio}})D(z_{\text{CMB}}). \quad (7)$$

The second set of data consists of photometric imaging from WISE *W1*. The full description of the data reduction process, from building mosaics to deriving the photometric parameters of interest, is given in section 2.4. The correction to apparent magnitudes is applied in the same manner as for the calibrated relation (K20):

$$m_{\text{cor}} = m_{\text{obs}} - A_{W1} - k_{W1} - I_{W1}, \quad (8)$$

where  $m_{\text{cor}}$  is the desired corrected magnitude,  $m_{\text{obs}}$  is the observed total magnitude,  $A_{W1}$  is the extinction correction due to dust from our own Galaxy (Schlegel et al. 1998),  $k_{W1}$  is the  $k$ -correction of the form  $A_{W1}^k = -2.27z$  (Oke & Sandage 1968; Huang et al. 2007), and  $I_{W1}$  is the correction for internal extinction which were considered but neglected because they are small in *W1* band. Sakai et al. (2000) parameterize them as  $\gamma \log a/b$ . If the effective wavelength of *W1* is  $3.4 \mu\text{m}$ , and the absorption in magnitudes is proportional to  $\lambda^{-1}$ , the maximum value is less than 0.1 mag for  $\log W = 2.5$ .

The absolute magnitude for each galaxy, for the purpose of visualizing the data only, was calculated as:

$$M = m_{\text{cor}} - 5 \log_{10}(D_L) - 25. \quad (9)$$

Figure 5 visualizes the three ingredients needed for the TFR: (A) the solid line denotes the calibrated TFR in WISE *W1* and the associated 1- $\sigma$  and 3- $\sigma$  regions (shaded areas); (B) the velocity width  $\log W_{\text{mx}}$ , on the  $x$ -axis is the maximum rotational velocity derived from the WALLABY spectra (Section 2.2); (C) the absolute magnitude  $M$ , on the  $y$ -axis is derived from Equation 9. The TFR fit is performed using the hyperfit method (Robotham & Obreschko 2015), allowing varying uncertainties in both axes.

We calculated the scatter about the TFR for the four WALLABY fields in Fig. 5. The rms for Hydra is  $0.90 \pm 0.08$  mag, which is comparable to the value of 0.89 found by K20 for the same cluster. The rms scatter in the Norma field is  $1.18 \pm 0.17$  mag which is slightly higher than most of the individual clusters in K20. The higher rms scatter in the TFR in Norma field is due to the strong dust extinction and stellar confusion which affects the photometric data reduction. The scatter about the TFR in Eridanus field is  $0.58 \pm 0.08$  mag which is the smallest of all the four fields and is identical to the rms scatter of the final calibrated TFR from K20. The rms scatter about the TFR in the NGC4636 region is the highest at  $1.61 \pm 0.19$  mag. The source of this scatter may be the noisy WALLABY spectra with baseline ripples due to residuals caused by strong radio continuum sources in the NGC4636 field (see Fig. 3).

Furthermore, source finding in the N4636 group was done in a different way from the other fields (Hydra, Norma and Eridanus). It was done by searching at the coordinates (RA, Dec,  $z$ ) of previously catalogued galaxies, while the source finding for the other clusters was done blindly. The master catalogue providing input coordinates

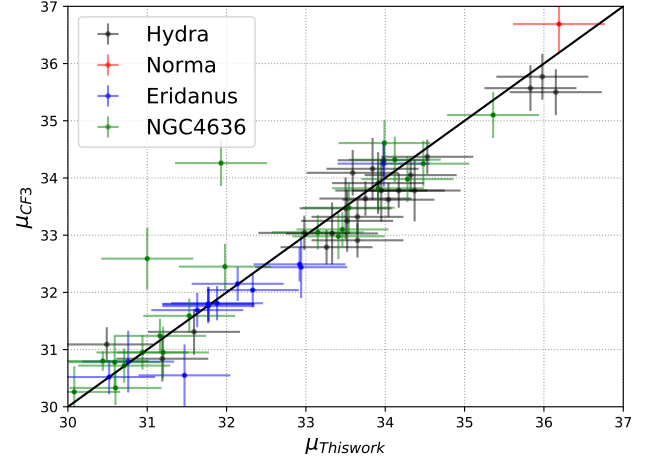


Figure 6. Comparison of the distance modulus measurements from the WALLABY pre-pilot survey (this work) vs. CosmicFlows-3 (Tully et al. 2016)

for NGC4636 was a combination of SDSS, ALFALFA, HIPASS and 6dFGS. Moreover the northern tile of the NGC 4636 field consists of only a single footprint, as the other footprint had to be discarded due to data quality issues. Hence, the noise level in the northern half of the field is significantly higher than in all other fields.

With all parameters in hand, the absolute magnitude of each galaxy is calculated in this article using the slope and zero point provided in K20 given its maximum rotational velocity :

$$M(W_{\text{mx}}) = -(20.36 \pm 0.07) - (9.47 \pm 0.14)(\log_{10} W_{\text{mx}} - 2.5) - 2.699, \quad (10)$$

where the TFR slope is  $(-9.47 \pm 0.14)$ , the zero point is  $(-20.36 \pm 0.07)$ , and the conversion of the AB to the Vega system is 2.699.

Using the apparent and absolute magnitude derived from equations 8 & 10, we can calculate the distance modulus as:

$$\mu = m_{\text{cor}} - M(W_{\text{mx}}). \quad (11)$$

Cross-matching with the CosmicFlows-3 (CF3) catalog (Tully et al. 2016) result in 24 source matches in Hydra, 1 in Norma, 13 in Eridanus, and 24 in the NGC4636 field. We compared our measurements for the distance modulus to the published ones from CF3. Figure 6 shows the comparison of the distance modulus from the four WALLABY fields with the ones from CF3. Figure 6 shows that our measurements appear to be systematically higher than the CF3 distance moduli measurements. This can be due to the value of the zero point calibration which was adjusted for the CF3 measurements specifically, but not for our WALLABY measurements. The zero point calibration will not be an issue for WALLABY measurements in the future, given the large sky-area which will allow it to easily be adjusted using more accurate measurements such as SN Ia.

The distribution of the measured TF distances in the four WALLABY fields are shown in Fig. 7. The WALLABY Hydra field includes background galaxies that do not belong to the Hydra cluster. The same applies to the Norma and Eridanus fields. Measuring distances to the Hydra, Norma, NGC 4636 and Eridanus clusters will therefore require restrictions on redshift.

Fortunately, there is a clear distinction in the redshift distribution between the galaxies in the cluster and the background galaxies in the

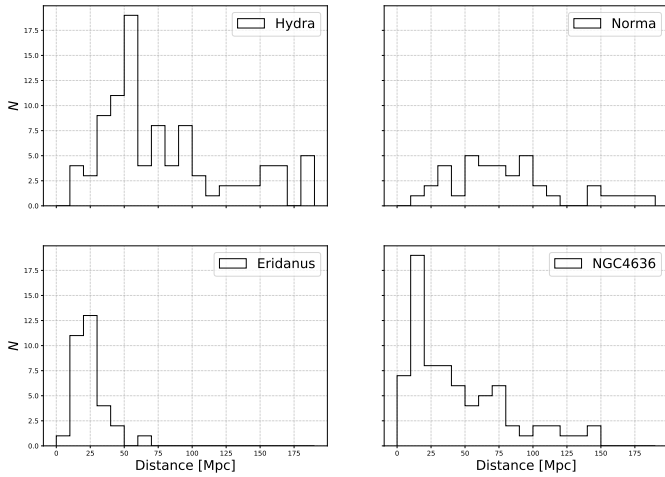


**Figure 7.** TFR distance distribution of galaxies in the four fields after extinction and k-corrections and the b/a cut  $< 0.7$  using K20 calibration.

Hydra, Norma, and Eridanus fields. Figure 8 shows the redshift distribution in the four WALLABY fields. The dashed-red lines represent the distinction line between the cluster galaxies and the background ones. Using only galaxies with redshifts in the low-redshift side of the dashed-red lines, we measured the weighted average distance to Hydra, Norma, NGC 4636 and Eridanus to be  $53.5 \pm 2.5$ ,  $69.4 \pm 5.5$ ,  $23.0 \pm 2.1$  and  $21.5 \pm 1.4$  Mpc, respectively. In this study, the Norma distance refers to the eastern overdensity (which is part of the Norma supercluster). This distance may be slightly different from the cluster distance due to filament projection. In the next section a comparison with previous determinations of these distances will be made.

Peculiar velocities are the non-Hubble velocities induced gravitationally by large scale structure. For a Hubble Constant between 68 and 73 km/s/Mpc the peculiar velocities with respect to the CMB of the Hydra, Norma, NGC 4636 and Eridanus clusters lie in the range  $(-320, -40)$ ,  $(-730, -350)$ ,  $(300, 430)$  and  $(0, 110)$  km s $^{-1}$  respectively.

#### 4 SPATIAL DISTRIBUTION OF GALAXIES IN THE PHASE 1 PILOT SURVEY

Figure 8 illustrates the variance in the redshift distribution between the WALLABY pilot survey fields and the presence of cluster foreground and background galaxies. It also shows that the pilot integration times allow us to reach a recessional velocity of 15,000 km s $^{-1}$ , doubling what has been achieved by predecessor all-sky surveys reliant on single dish observations, such as 2MTF. These higher redshifts have so far only been accessible using fundamental plane techniques – e.g. 6dFGS, which provides about 6,000 useful peculiar velocities. WALLABY is expected to deliver about 30,000-50,000 peculiar velocities.

##### 4.1 Hydra and Norma cluster fields

The Hydra cluster has a mean redshift of 0.012 (Babyk & Vavilova 2013) and a velocity dispersion of 690 km s $^{-1}$  (Lima-Dias et al. 2021). Figure 8 shows the redshift distribution for Hydra cluster galaxies in our sample whereas Fig. 5 shows the TFR for these galaxies.

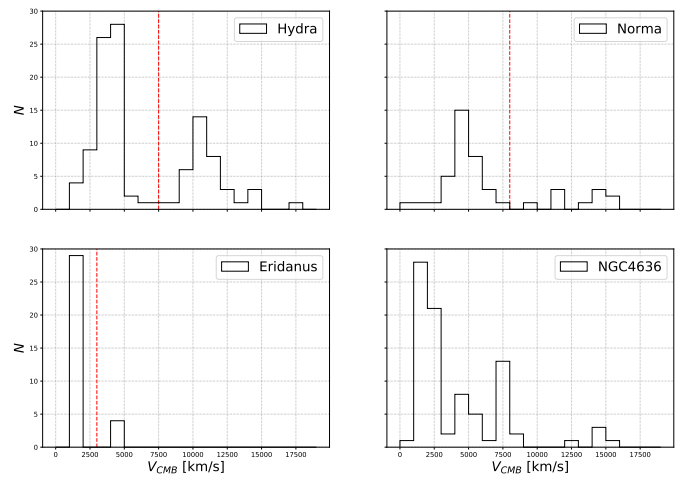


**Figure 8.** The redshift distribution (CMB frame) of all 614 galaxies in the Hydra, Norma, Eridanus and NGC4636 fields. The dashed-red lines in the Hydra, Norma and Eridanus plots represent the estimated division between the cluster and background galaxies. The WALLABY pilot integration time allows the detection of galaxies located at 15,000 km s $^{-1}$ , around twice the distance limit of previous single dish surveys such as HIPASS.

Woudt et al. (2008) find a mean velocity of  $4871 \pm 54$  km s $^{-1}$  for the Norma cluster and locate its centre at  $(l, b) = (325.3^\circ, -7.2^\circ)$ . They identify it as the richest cluster in the region of the Great Attractor. Mutabazi (2021), in a study of its fundamental plane, finds a small peculiar velocity. The WALLABY pilot survey field is centred on  $(l, b) = (329.3^\circ, -10.4^\circ)$ , i.e.  $5.1^\circ$ , respectively 6 Mpc from the cluster center. Nevertheless, there is clear overdensity of galaxies visible at the cluster redshift (Fig. 8).

A full 3D view of the Great Attractor region with the first CosmicFlows reconstruction of the local velocity field near Norma and Hydra clusters was presented by Courtois et al. (2012). Infall to the Norma cluster takes the form of a sharper distribution in redshift space than in real space (see Fig. 9).

The positions of WALLABY galaxies within the Cosmic Web can be studied using the full matter (dark and luminous) density contrast field (usually noted  $\delta$ ) reconstructed from the CosmicFlows-3 Catalog of peculiar velocities (Graziani et al. 2019; Tully et al. 2019; Courtois et al. 2019; Pomarède et al. 2020). Figure 9 shows the redshift locations of galaxies of the Norma survey versus a real-space three-dimensional visualization of the overdensity field, restricted to a slice. The visualization is obtained by a combination of a ray-casting algorithm (Pomarède et al. 2017a) resulting in a smooth rendering of the  $\delta$  overdensity field ranging from most underdense (deep blue colour) to most overdense (yellow), and a series of semi-transparent isosurface polygons resulting in a sharp materialization of the surfaces ranging from  $\delta = 0$  (grey surface) to highly overdense ( $\delta = 2.8$  in red). The grey surface hence marks the frontier between the underdense and the overdense Universe. The most noticeable feature in the distribution of WALLABY galaxies is their aggregation near the Norma cluster at  $SGX \approx -5000$  km s $^{-1}$ , seen as a pronounced local maximum in the density contrast field ( $\delta$  field). Between the Local Group and the Norma cluster, the field includes a section of the Local Void (Tully et al. 2019) and the termination of a filament connecting the Fornax cluster to the Norma cluster, as can better be seen from the interactive 3D visualization supplementing Fig. 9 (see



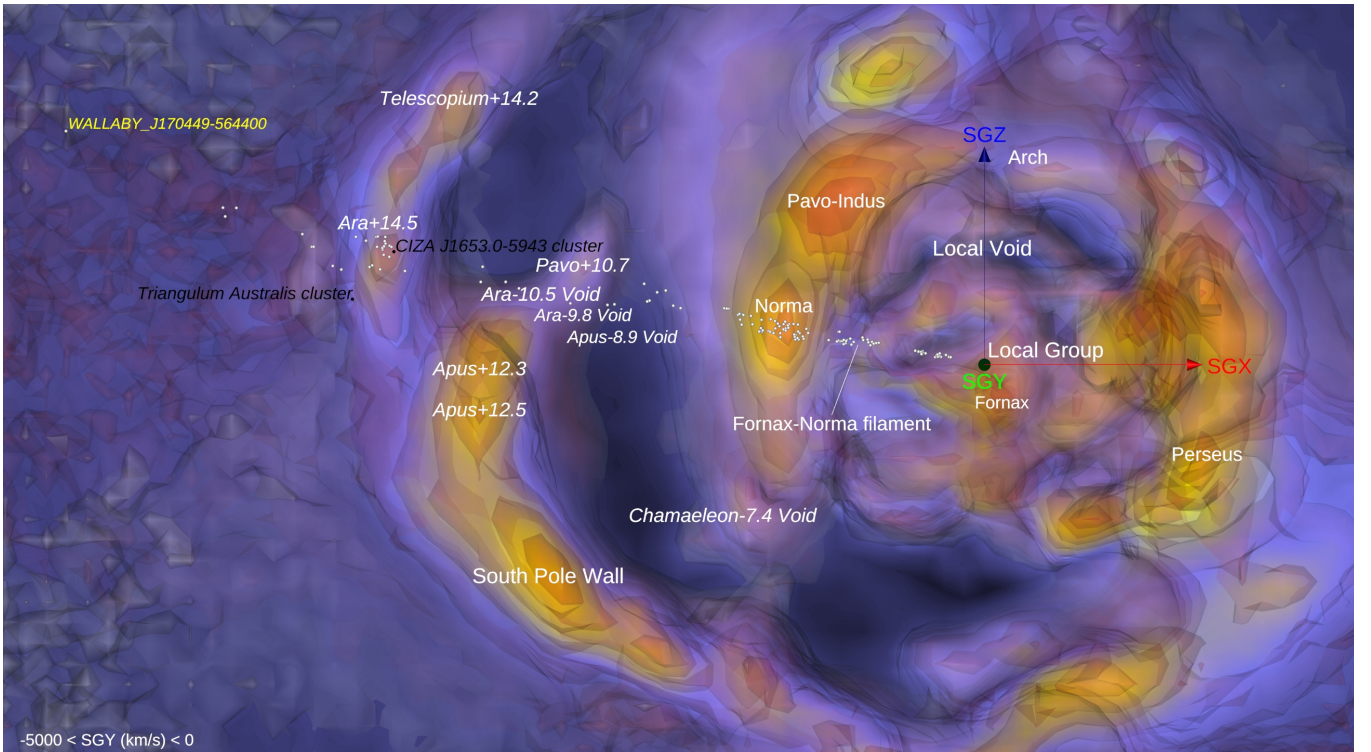


**Figure 9.** Map of the redshift positions of galaxies in the Norma field (white points) overlaid on the (coloured) density contrast field ( $\delta$ ) as reconstructed from the CosmicFlows-3 Catalog of peculiar velocities. Scale and orientation are provided by the red and blue  $5000 \text{ km s}^{-1}$ -long arrows emanating from our position and associated with the supergalactic coordinates SGX and SGY, respectively. A slice defined by  $0 > \text{SGY} > -5000 \text{ km s}^{-1}$  is here seen from the negative SGY direction. This static view is complemented by an online [interactive 3D visualization of the Norma survey field](#) showing three levels of the overdensity  $\delta$ , field. This tool can be used to better grasp how the field includes a series of voids and overdensities.

annotations 2 and 3). Beyond the Norma-Pavo-Indus filament (Fairall 1998; Courtois et al. 2013), the field includes the void separating this filament and the South Pole Wall (Pomarède et al. 2020). The map of Fig. 9 indicates the location of local extrema of the over and under-density field  $\delta$ , such as the Ara-10.5 Void and the Ara+14.5 overdensity, whose names include the name of the constellation in which they sit, followed by a ‘+’ for an overdensity or a ‘-’ for an underdensity, followed by their redshift in units of  $1000 \text{ km s}^{-1}$ , a convention established in Tully et al. (2019). An aggregation of WALLABY galaxies is found at the location of the Ara+14.5 knot of the Cosmic Web, that is nearly coincident with the CIZA J1653.0-5943 cluster (Ebeling et al. 2002). Beyond this most distant section of the South Pole Wall, the field presumably enters a new void, in regions where the CosmicFlows-3 reconstruction tends to a null field due lack of sufficient data. The most distant galaxy in the Norma field, located at redshift 0.073, is indicated on the map.

In Fig. 10 the distribution of the WALLABY galaxies in the Hydra field is plotted in a similar way on top of the CosmicFlows-3 cosmography. The density of WALLABY galaxies as a function of distance displays contrasting features: after displaying a handful of galaxies located in our vicinity at  $\approx 900 \text{ km s}^{-1}$ , no galaxies are detected in the void located in the foreground of the Hydra cluster. A major aggregation of objects is then seen at the crossing of the Hydra cluster, which is part of a high-density node in the Cosmic Web, as seen in the map of the CosmicFlows-3 density contrast. In the background of the Hydra cluster, the surveyed region includes a deep void (Hydra-7.4) where very few galaxies reside. In the background of this void, there

is an extended cloud of galaxies scattered throughout a wall located in Hydra at about  $10,000 \text{ km s}^{-1}$ , where local maxima in the density are found: Hydra+9.7, Hydra+9.9 and Antlia+8.8. After dropping as a function of distance, the number density of galaxy rises again at the most extreme distances, with WALLABY J104910-282305 being the most remote one at  $\sim 23,000 \text{ km s}^{-1}$ . This infall pattern of peculiar velocities leads to a higher overdensity in redshift space (Fig. 8) than in real space (Fig. 7).

#### 4.2 The NGC 4636 cluster and Eridanus fields

The spatial distribution of the galaxies of the NGC 4636 survey is shown in Fig. 11. The highest density in the field is at the crossing of the Virgo Strand (Courtois et al. 2013), a section of the Cen-Vir-PP filament that connects the Centaurus and Perseus nodes of the Cosmic Web through the Virgo cluster (Pomarède et al. 2017b), in which the NGC 4636 cluster is nested. Beyond the cluster, the field includes the outskirts of the void located between Virgo and the Great Wall (Gregory & Thompson 1978), and also includes part of the Centaurus-Coma filament (Pomarède et al. 2017b). The number of galaxies then rises at the intersection of the Great Wall (de Lapparent et al. 1986) near the Virgo+6.3 and Virgo+7.1 local maxima of the density contrast. In the background of the Great Wall, there is the trough and peak of Virgo-10.3 and Virgo+14.5.

Finally, the location of the galaxies of the Eridanus super group survey is presented in Fig. 12. It shows that the galaxies are found near the Fornax node in the Cosmic Web, and distributed along

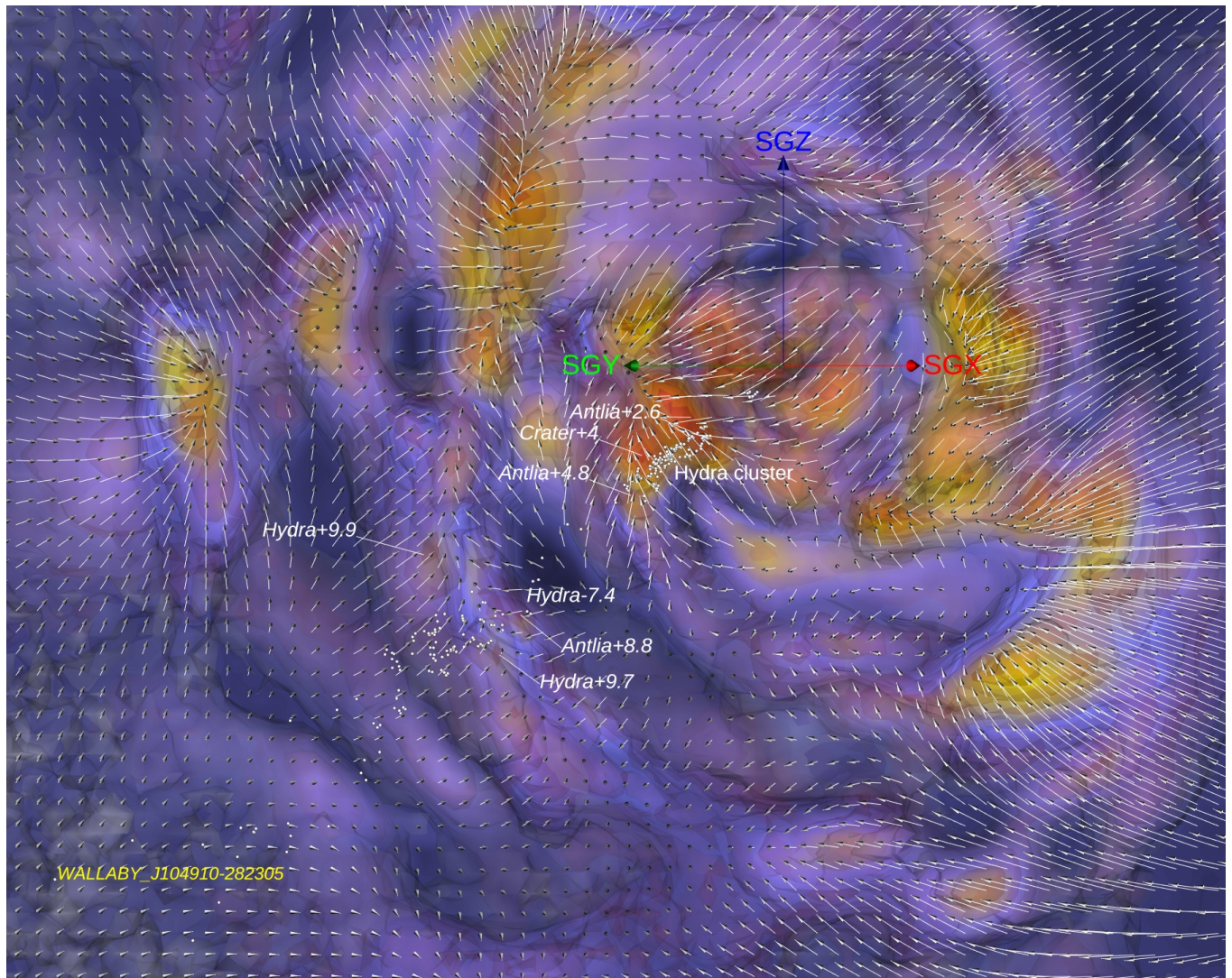


**Figure 10.** Map of the redshift positions of galaxies in the Hydra field (white points) overlaid on the (coloured) full matter (dark + luminous) density contrast  $\delta$ , field and the peculiar (gravitational) velocity field (white arrows) as reconstructed from the CosmicFlows-3 Catalog. Scale and orientation are provided by the red, green and blue  $5000 \text{ km s}^{-1}$ -long arrows emanating from our position and associated with the three cardinal axes of the supergalactic coordinate system SGX, SGY, and SGZ, respectively. A slice of  $5000 \text{ km s}^{-1}$ -thickness centered on the plane defined by the supergalactic longitude of the Hydra cluster ( $\text{SGL}=139.36^\circ$ ) is here seen face-on. This static view is complemented by an online [interactive 3D visualization of the Hydra survey beam](#) showing three levels of the overdensity  $\delta$ , field. This tool can be used to better grasp how the field includes a series of voids and overdensities.

the density gradient seen in the transition toward the Sculptor Void located in the background (Pellegrini et al. 1990; Fairall 1998).

### 4.3 Discussion

The cosmographic maps presented in the previous section demonstrate that the WALLABY pilot survey fields probe a vast diversity of elements of the cosmic web: intersecting numerous features such as voids, filaments, walls, and the nodes which host the targeted clusters. The future inclusion of WALLABY-detected galaxies in the CosmicFlows collection will add useful data for cosmographical purposes. Of particular interest are the regions around the Hydra and Norma clusters and their roles in the dynamical structure and influence of the Great Attractor (Dressler et al. 1987; Woudt et al. 2008; Tully et al. 2014; Hoffman et al. 2017). WALLABY has the advantage

of being able to peer through the Galactic Plane, permitting the study of the so-called Zone of Avoidance which limits optical/IR surveys. Also of great interest are galaxies that reside in voids, which will provide improved constraints on the flows evacuating these underdense patches (Tully et al. 2008; Rizzi et al. 2017; Shaya et al. 2017). The most distant sections of the pilot fields, with velocities out to  $22,000 \text{ km s}^{-1}$ , will bring in new useful information on the architecture of the Cosmic Web in remote locations, thus providing better measurements of the large-scale gravitational field than currently available and potentially providing a definitive explanation for the amplitude of the CMB dipole.

In the vicinity of the Great Attractor, peculiar velocities for the Hydra and Norma fields show an infall pattern towards the respective clusters, i.e. positive peculiar velocities on the nearside of the clusters and negative on the far side. Beyond Hydra, positive velocities return

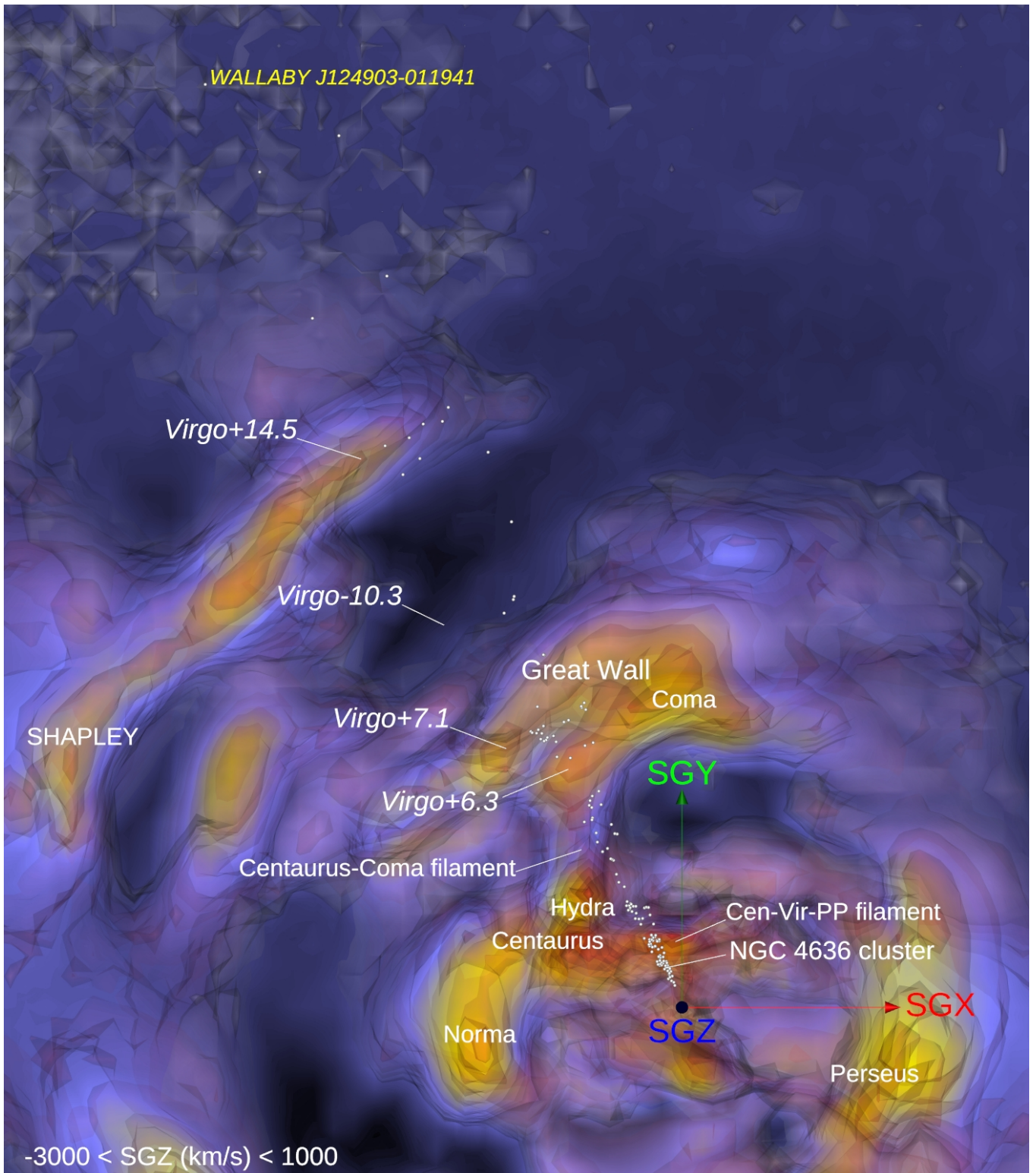


**Figure 11.** Map of the redshift positions of galaxies in the NGC 4636 field (white points) overlaid on the (coloured) density contrast  $\delta$ , as reconstructed from the CosmicFlows-3 Catalog of peculiar velocities. Scale and orientation are provided by the red and green  $5000 \text{ km s}^{-1}$ -long arrows emanating from our position and associated with supergalactic coordinates SGX and SGY, respectively. A slice contained defined by  $1000 > \text{SGZ} > -3000 \text{ km s}^{-1}$  is here seen from the positive SGZ direction. This static view is complemented by an online [interactive 3D visualization of the NGC 4636 survey field](#).

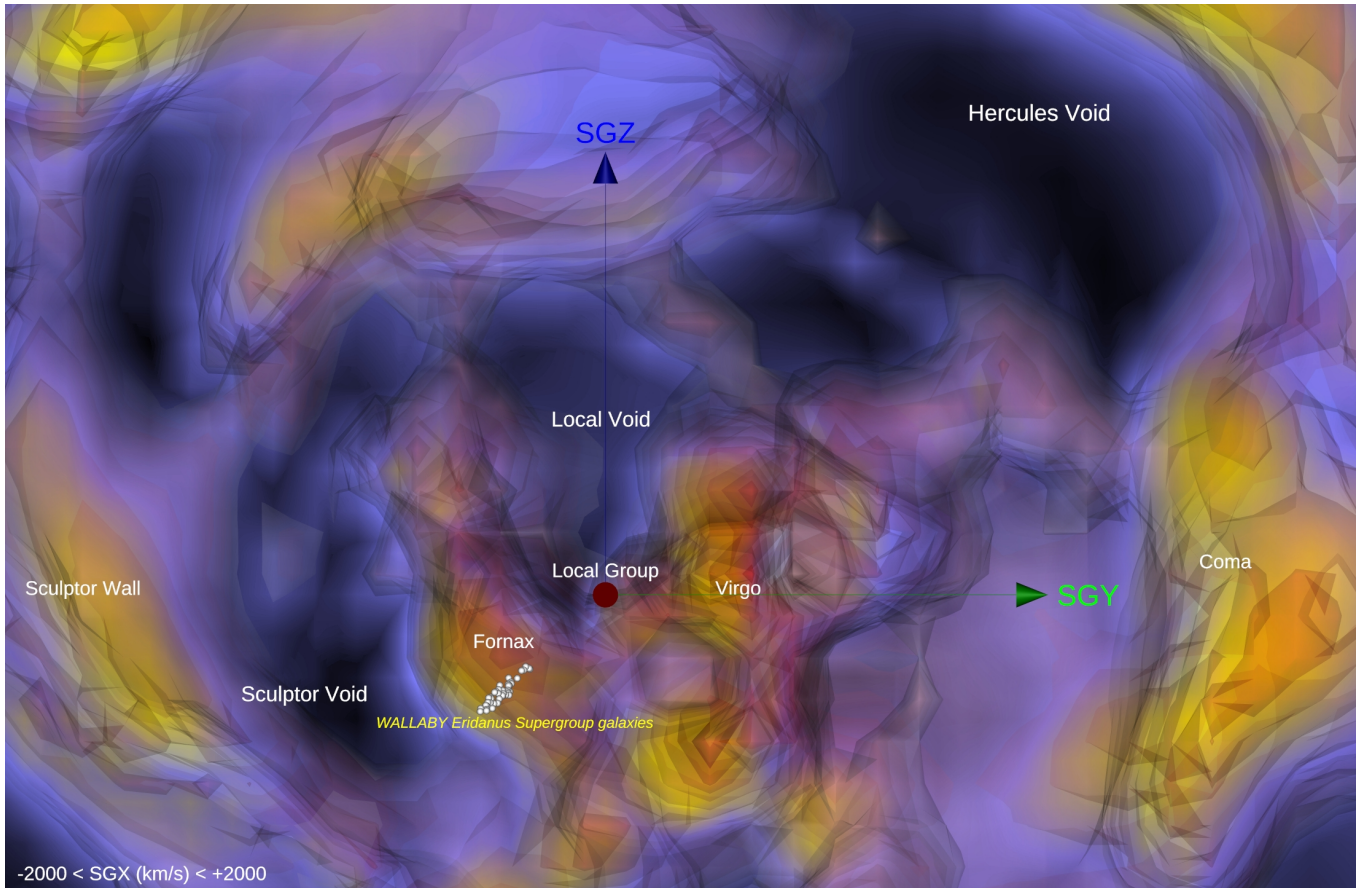


**Figure 12.** Map of the redshift positions of galaxies in the Eridanus super group (white points) overlaid on the (coloured) density contrast  $\delta$ , as reconstructed from the CosmicFlows-3 Catalog of peculiar velocities. Scale and orientation are provided by green and blue 5000  $\text{km s}^{-1}$ -long arrows emanating from our position and associated with supergalactic coordinates SGY and SGZ, respectively. A slice defined by  $2000 > \text{SGX} > -2000 \text{ km s}^{-1}$  is here seen from the positive SGX direction. This static view is complemented by an online [interactive 3D visualization of the Eridanus super group survey](#).

as the galaxies come under the influence of the wall located at about  $10,000 \text{ km s}^{-1} \approx 135 \text{ Mpc}$ , seen in Fig. 10 at the locations of the local maxima Hydra+9.7 and Hydra+9.9. The pattern observed in the peculiar velocities at  $\sim 100 \text{ Mpc}$  is typical of an evacuation by the void located at  $7400 \text{ km s}^{-1}$ , labelled Hydra-7.4 in Fig. 10, where galaxies located in the foreground of this void have negative velocities, while galaxies located in the background have positive velocities. The wealth of data represented by the WALLABY galaxies located in this direction at large distance will play an important role in mapping the structure currently hinted at by the CosmicFlows-3 reconstruction, in particular of the wall seen in Hydra at  $10,000 \text{ km s}^{-1}$ .

## 5 CONCLUSIONS

The Tully-Fisher distance of the Eridanus group is  $21.5 \pm 1.4 \text{ Mpc}$ , and its peculiar velocity for a Hubble constant of  $68\text{--}73 \text{ km s}^{-1} \text{ Mpc}^{-1}$  is small, between 0 and  $110 \text{ km s}^{-1}$ . The NGC 4636 group is a complex structure within the Virgo cluster zero velocity surface, and its Tully-Fisher distance is  $23.0 \pm 2.1 \text{ Mpc}$ . Under the same assumptions its peculiar velocity is  $300\text{--}430 \text{ km s}^{-1}$ . The distance of the Hydra cluster is  $53.5 \pm 2.5 \text{ Mpc}$ . There is a substantial background group associated with the Shapley Supercluster. We measure

a peculiar velocity of  $-320$  to  $-40 \text{ km s}^{-1}$  for the Hydra cluster, assuming  $68 < H_0 < 73 \text{ km s}^{-1} \text{ Mpc}^{-1}$ . The Norma cluster is the most distant in the present sample at  $69.4 \pm 5.5 \text{ Mpc}$ . Its peculiar velocity is  $-350$  to  $-730 \text{ km s}^{-1}$  under the same assumptions.

This study also aims at testing the reliability, accuracy and dynamic range in distance able to be provided by Tully-Fisher distances for galaxies detected and parameterised in the pre-pilot and Phase 1 surveys of WALLABY. It is also a prediction for what the full survey will deliver. We find that :

- Measurements of galaxy velocity widths are in excellent agreement with those measured using previous single-dish observations with typical discrepancies around  $7 \text{ km s}^{-1}$ , validating both the data quality and observational strategy of WALLABY. The WALLABY Tully-Fisher distances have uncertainties at the level of 5 to 10% which are similar or better than the accuracy obtained with single dish observations.

- Even as close to the Zone of Avoidance as the Norma cluster, HI spectra provided by the SoFiA pipeline are excellent and extinction in the WISE W1 band is less than 0.1 mag. The combination of WALLABY and WISE W1 band observations will enable investigation of large number of accurate peculiar velocities of galaxies in the upcoming full WALLABY survey. The Tully-Fisher dispersion

obtained is at the level of 0.9 unit which is excellent for these cluster fields.

- The distribution of galaxies and kinematic pattern in the Hydra and Norma fields is one of infall to the cluster mass concentrations.
- The WALLABY pilot survey sensitivity and widefield capability will extend the investigation of peculiar velocities beyond what was previously achieved with the single dish TFR method. WALLABY will detect about 500k galaxies at a mean redshift of  $z = 0.05$ . If 251 out of 614 of the pilot phase 1 galaxies pass the S/N and inclination tests, this might suggest that 200k Tully-Fisher distances would result from WALLABY – much higher than was expected in initial proposals and increasing by a factor of twenty the current number of Tully-Fisher distances in Cosmic-Flows-4. The number may be slightly optimistic given that we only observed nearby structures on Phase 1. However, most fields should have their peak redshift at 0.04, well beyond these local structures.

## ACKNOWLEDGEMENTS

The Australian SKA Pathfinder is part of the Australia Telescope National Facility which is managed by CSIRO. Operation of ASKAP is funded by the Australian Government with support from the National Collaborative Research Infrastructure Strategy. ASKAP uses the resources of the Pawsey Supercomputing Centre. Establishment of ASKAP, the Murchison Radio-astronomy Observatory and the Pawsey Supercomputing Centre are initiatives of the Australian Government, with support from the Government of Western Australia and the Science and Industry Endowment Fund. We acknowledge the Wajarri Yamatji people as the traditional owners of the Observatory site. Parts of this research were supported by the Australian Research Council Centre of Excellence for All Sky Astrophysics in 3 Dimensions (ASTRO 3D), through project number CE170100013. We would like to thank all our colleagues on the WALLABY team for helpful discussions. We have made use of NASA data products, including WISE and NED, and also NSF OIR Lab data products. We acknowledge the use of the HyperLeda database. HC is grateful to the Institut Universitaire de France and CNES for its support. KS, CH, and TD are supported by the Australian Government through the Australian Research Council's Laureate Fellowship funding scheme (project FL180100168). AD acknowledges financial support from the Project IDEXLYON at the University of Lyon under the Investments for the Future Program (ANR-16-IDEX-0005). AB acknowledges support from the Centre National d'Etudes Spatiales (CNES), France. DK acknowledges funding from the European Research Council (ERC) under the European Union's Horizon 2020 research and innovation programme (grant agreement no. 679627; project name FORNAX). RCKK is supported by the South African Research Chairs Initiative of the Department of Science and Technology and National Research Foundation. FB acknowledges funding from the European Research Council (ERC) under the European Union's Horizon 2020 research and innovation programme (grant agreement No.726384/Empire). AD is supported by a KIAS Individual Grant (PG087201) at Korea Institute for Advanced Study. Many thanks to Dmitry Makarov for helping us on the cross-identification with galaxy PGC names.

## REFERENCES

Aaronson M., Huchra J., Mould J., 1979, *ApJ*, **229**, 1  
 Babyk I. V., Vavilova I. B., 2013, *Odessa Astronomical Publications*, **26**, 175  
 Cluver M. E., et al., 2014, *ApJ*, **782**, 90

Cluver M. E., Jarrett T. H., Dale D. A., Smith J. D. T., August T., Brown M. J. I., 2017, *ApJ*, **850**, 68  
 Courtois H. M., Tully R. B., 2015, *MNRAS*, **447**, 1531  
 Courtois H. M., Tully R. B., Fisher J. R., Bonhomme N., Zavodny M., Barnes A., 2009, *AJ*, **138**, 1938  
 Courtois H. M., Tully R. B., Makarov D. I., Mitronova S., Koribalski B., Karachentsev I. D., Fisher J. R., 2011a, *MNRAS*, **414**, 2005  
 Courtois H. M., Tully R. B., Héraudeau P., 2011b, *MNRAS*, **415**, 1935  
 Courtois H. M., Hoffman Y., Tully R. B., Gottlöber S., 2012, *ApJ*, **744**, 43  
 Courtois H. M., Pomarède D., Tully R. B., Hoffman Y., Courtois D., 2013, *AJ*, **146**, 69  
 Courtois H. M., Kraan-Korteweg R. C., Dupuy A., Graziani R., Libeskind N. I., 2019, *MNRAS*, **490**, L57  
 Dressler A., Faber S. M., Burstein D., Davies R. L., Lynden-Bell D., Terlevich R. J., Wegner G., 1987, *ApJ*, **313**, L37  
 Ebeling H., Mullis C. R., Tully R. B., 2002, *ApJ*, **580**, 774  
 Fairall A. P., 1998, *Large-scale structures in the universe* / Anthony P. Fairall. New York : Wiley, 1998.. Wiley-Praxis series in astronomy and astrophysics  
 Fernie J. D., 1969, *PASP*, **81**, 707  
 For B. Q., et al., 2021, *MNRAS*, **507**, 2300  
 Giovanelli R., Haynes M. P., Herter T., Vogt N. P., da Costa L. N., Freudling W., Salzer J. J., Wegner G., 1997, *AJ*, **113**, 53  
 Graziani R., Courtois H. M., Lavaux G., Hoffman Y., Tully R. B., Copin Y., Pomarède D., 2019, *MNRAS*, **488**, 5438  
 Gregory S. A., Thompson L. A., 1978, *ApJ*, **222**, 784  
 Haynes M. P., et al., 2018, *ApJ*, **861**, 49  
 Hoffman Y., Courtois H. M., Tully R. B., 2015, *MNRAS*, **449**, 4494  
 Hoffman Y., Pomarède D., Tully R. B., Courtois H. M., 2017, *Nature Astronomy*, **1**, 0036  
 Hong T., et al., 2019, *MNRAS*, **487**, 2061  
 Hotan A. W., et al., 2021, *Publ. Astron. Soc. Australia*, **38**, e009  
 Huang J. S., et al., 2007, *ApJ*, **664**, 840  
 Jarrett T. H., et al., 2012, *The Astronomical Journal*, **144**, 68  
 Jarrett T. H., et al., 2013, *AJ*, **145**, 6  
 Jarrett T. H., Cluver M. E., Brown M. J. I., Dale D. A., Tsai C. W., Masci F., 2019, *ApJS*, **245**, 25  
 Koribalski B. S., et al., 2004, *AJ*, **128**, 16  
 Koribalski B. S., et al., 2020, *Ap&SS*, **365**, 118  
 Kourkchi E., Tully R. B., Neill J. D., Seibert M., Courtois H. M., Dupuy A. r., 2020a, *ApJ*, **884**, 82  
 Kourkchi E., et al., 2020b, *ApJ*, **902**, 145  
 Lagattuta D. J., Mould J. R., Staveley-Smith L., Hong T., Springob C. M., Masters K. L., Koribalski B. S., Jones D. H., 2013, *ApJ*, **771**, 88  
 Lima-Dias C., et al., 2021, *MNRAS*, **500**, 1323  
 Meyer M. J., et al., 2004, *MNRAS*, **350**, 1195  
 Mould J., 2020, *Frontiers in Astronomy and Space Sciences*, **7**, 21  
 Mutabazi T., 2021, *ApJ*, **911**, 16  
 Neill J. D., Seibert M., Tully R. B., Courtois H., Sorce J. G., Jarrett T. H., Scowcroft V., Masci F. J., 2014, *ApJ*, **792**, 129  
 Oke J. B., Sandage A., 1968, *ApJ*, **154**, 21  
 Pellegrini P. S., da Costa L. N., Huchra J. P., Latham D. W., Willmer C. N. A., 1990, *AJ*, **99**, 751  
 Peterson E. R., et al., 2021, arXiv e-prints, p. arXiv:2110.03487  
 Planck Collaboration et al., 2020, *A&A*, **641**, A1  
 Pomarède D., Courtois H. M., Hoffman Y., Tully R. B., 2017a, *PASP*, **129**, 058002  
 Pomarède D., Hoffman Y., Courtois H. M., Tully R. B., 2017b, *ApJ*, **845**, 55  
 Pomarède D., Tully R. B., Graziani R., Courtois H. M., Hoffman Y., Lezmy J., 2020, *ApJ*, **897**, 133  
 Ponomareva A. A., et al., 2021, *MNRAS*, **508**, 1195  
 Rizzi L., Tully R. B., Shaya E. J., Kourkchi E., Karachentsev I. D., 2017, *ApJ*, **835**, 78  
 Robotham A. S. G., Obreschkow D., 2015, *Publ. Astron. Soc. Australia*, **32**, e033  
 Said K., Kraan-Korteweg R. C., Staveley-Smith L., Williams W. L., Jarrett T. H., Springob C. M., 2016, *MNRAS*, **457**, 2366

- Said K., Colless M., Magoulas C., Lucey J. R., Hudson M. J., 2020, *MNRAS*, **497**, 1275
- Sakai S., et al., 2000, *ApJ*, **529**, 698
- Schlegel D. J., Finkbeiner D. P., Davis M., 1998, *ApJ*, **500**, 525
- Serra P., et al., 2015, *MNRAS*, **448**, 1922
- Shaya E. J., Tully R. B., Hoffman Y., Pomarède D., 2017, *ApJ*, **850**, 207
- Sorce J. G., et al., 2013, *ApJ*, **765**, 94
- Springel V., et al., 2018, *MNRAS*, **475**, 676
- Thévenot M., Cornen C., Goodwin B. L., Macmillan C., Stenner A. G., Téglás B., 2020, *Research Notes of the American Astronomical Society*, **4**, 159
- Tully R. B., Fisher J. R., 1977, *A&A*, **54**, 661
- Tully R. B., Fouqué P., 1985, *ApJS*, **58**, 67
- Tully R. B., Shaya E. J., Karachentsev I. D., Courtois H. M., Kocevski D. D., Rizzi L., Peel A., 2008, *ApJ*, **676**, 184
- Tully R. B., Courtois H., Hoffman Y., Pomarède D., 2014, *Nature*, **513**, 71
- Tully R. B., Courtois H. M., Sorce J. G., 2016, *AJ*, **152**, 50
- Tully R. B., Pomarède D., Graziani R., Courtois H. M., Hoffman Y., Shaya E. J., 2019, *ApJ*, **880**, 24
- Wang J., et al., 2021, *ApJ*, **915**, 70
- Westmeier T., et al., 2021, *MNRAS*, **506**, 3962
- Wong O. I., et al., 2021, *MNRAS*, **507**, 2905
- Woudt P. A., Kraan-Korteweg R. C., Lucey J., Fairall A. P., Moore S. A. W., 2008, *MNRAS*, **383**, 445
- Wright E. L., et al., 2010, *AJ*, **140**, 1868
- de Lapparent V., Geller M. J., Huchra J. P., 1986, *ApJ*, **302**, L1

**APPENDIX A: DATA**

Tables in Appendix A present four catalogs of Hydra, Norma, Eridanus, and NGC4636. The parameters listed in the catalogs are:

Column (1) - WALLABY ID as reported in the WALLABY Pilot Survey data release (Westmeier et al., in prep.).

Columns (2) - Principal Galaxies Catalogue number (PGC)

Columns (3 and 4) - Right Ascension (RA) and Declination (Dec.) in the J2000.0 epoch of the fitted position in WALLABY.

Column (5) - WISE W1 total magnitude after Galactic extinction and k corrections.

Column (6) - Inclination calculated from WISE ( $b/a$ ) as in equation 5.

Column (7) - Linewidths corrected for inclination.

Column (8) - CMB redshifts.

Column (9) - Tully-Fisher luminosity distances in Mpc.

Column (10 and 11) - Distance modulus and associated error.

Table A1: Hydra HI data from WALLABY phase 1 pilot survey.

Name	PGC	RA	DEC	$W_{1_{tot}}$	$i$	$W_{mx}$	$z_{cmb}$	$d_L$	$\mu$	$e_\mu$
J100342-270137	29166	150.9256	-27.0271	10.715	79.3316	185.2012	0.00430152	20.0	31.5	0.58
J100351-273417	29179	150.9662	-27.5715	8.947	51.0182	421.9486	0.01043229	42.1	33.12	0.58
J100426-282638	29216	151.1091	-28.4442	9.9561	73.1772	202.6735	0.00471975	16.7	31.12	0.58
J100640-273917	29378	151.667	-27.6549	12.923	62.8353	223.6714	0.01536106	79.0	34.49	0.58
J100808-260942	29470	152.0353	-26.1618	13.4138	57.4373	132.8899	0.01141974	36.9	32.84	0.58
J100830-262140	768685	152.1256	-26.3611	14.5217	76.0108	118.515	0.01512221	49.5	33.47	0.58
J100939-290112	154738	152.4128	-29.0202	12.4737	47.9538	278.7484	0.0480433	97.4	34.94	0.58
J101025-275214	748738	152.6054	-27.8708	13.1662	68.9346	132.8803	0.00919987	33.0	32.59	0.58
J101208-252000	154861	153.0362	-25.3335	12.2087	58.4722	305.026	0.04684504	102.3	35.05	0.58
J101221-254604	29719	153.0904	-25.7678	11.4898	60.6661	430.1545	0.03330433	140.9	35.74	0.58
J101247-275028	29743	153.1998	-27.8413	9.4937	76.0108	350.3921	0.00984753	38.1	32.9	0.58
J101247-291053	732369	153.1962	-29.1815	13.2847	61.97	267.361	0.03197037	130.8	35.58	0.58
J101348-273147	29821	153.4516	-27.5299	13.3432	57.7338	164.3848	0.00981759	53.5	33.64	0.58
J101357-262550		153.4904	-26.4308	15.1772	52.8182	102.9217	0.03382259	51.3	33.55	0.58
J101359-253824	29836	153.4964	-25.64	13.2213	71.1098	205.0435	0.01177462	76.9	34.43	0.58
J101359-274538		153.4978	-27.7607	15.9193	73.7025	70.8468	0.00969587	35.6	32.76	0.59
J101438-272431	29888	153.661	-27.4087	10.8963	54.1261	386.2726	0.01496544	87.4	34.71	0.58
J101441-285221	29892	153.6744	-28.8726	7.4814	71.9901	312.3018	0.00479612	12.1	30.42	0.58
J101448-285723	29903	153.7006	-28.9565	10.5448	72.9533	400.5999	0.01509413	79.7	34.51	0.58
J101526-264259	764730	153.8614	-26.7166	13.8652	47.6238	300.5138	0.03412958	213.3	36.64	0.58
J101531-292423	29945	153.8793	-29.4066	12.4099	66.2786	337.516	0.03173132	135.9	35.67	0.58
J101537-272427		153.9057	-27.4078	15.3554	49.2591	96.3481	0.01157047	49.1	33.46	0.58
J101632-291258		154.1373	-29.2163	13.0964	76.0108	176.2266	0.01514422	54.5	33.68	0.64
J101756-285557		154.4866	-28.9325	14.4099	67.8558	170.5825	0.03769535	93.8	34.86	0.58
J101834-281550	3753792	154.6456	-28.264	14.6891	47.6238	151.6106	0.04194573	85.3	34.65	0.59
J101920-264135	30161	154.8353	-26.6931	12.3029	56.6184	318.5536	0.04414246	116.0	35.32	0.58
J101927-264159	764945	154.8662	-26.6999	14.1879	50.3033	110.4705	0.00964968	37.2	32.85	0.58
J102017-253913	30216	155.0743	-25.6538	13.4071	51.6485	150.4681	0.01264661	46.6	33.34	0.58
J102019-285220	30218	155.0828	-28.8722	11.15	76.9694	429.0481	0.03237219	119.9	35.39	0.58
J102023-253050		155.0966	-25.514	15.3675	58.4722	132.569	0.01211333	90.4	34.78	0.58
J102030-260951	30234	155.1281	-26.1642	12.8541	48.6094	417.2113	0.0572516	249.2	36.98	0.58
J102100-273339	753130	155.2535	-27.5608	14.1518	55.7186	254.1508	0.03442685	177.2	36.24	0.58
J102115-250342	783072	155.3137	-25.0618	13.6738	52.5855	313.4991	0.03393395	211.6	36.63	0.58
J102233-294017	726509	155.6378	-29.6715	14.9756	47.6238	200.3425	0.02718859	165.0	36.09	0.58
J102328-253424	777390	155.8685	-25.5736	12.4153	68.5745	399.6161	0.04170041	187.7	36.37	0.58
J102338-264531	764220	155.9116	-26.7589	14.1452	53.9731	290.575	0.03581803	227.6	36.79	0.58
J102416-270241	760541	156.0683	-27.0448	14.424	47.4581	261.9494	0.03578983	212.7	36.64	0.58
J102430-290904	732726	156.1259	-29.1511	13.6075	54.5075	143.7009	0.01363351	46.8	33.35	0.58
J102439-274841	749549	156.1626	-27.8117	15.1621	49.5819	136.6024	0.01315652	87.1	34.7	0.58
J102600-280334		156.5018	-28.0597	15.2205	54.9633	173.4279	0.0375637	140.5	35.74	0.58
J102621-291150	732211	156.5886	-29.1973	13.6973	62.403	97.0405	0.01345127	23.2	31.83	0.58
J102637-264142	764986	156.6545	-26.6952	14.5557	57.7338	112.3494	0.0325455	45.5	33.29	0.59
J102643-261256	770222	156.6797	-26.2157	12.7449	51.6485	345.5666	0.03439577	165.9	36.1	0.58
J102747-283425		156.9461	-28.5738	15.4282	48.6909	238.2983	0.03272924	282.3	37.25	0.58
J102818-255446	773700	157.0764	-25.9129	16.0183	52.43	93.3625	0.01386497	62.8	33.99	0.58
J102934-261937	30912	157.3949	-26.3271	12.8164	47.2921	217.74	0.01427068	71.5	34.27	0.58
J103002-284116	738653	157.5091	-28.688	13.1147	61.3915	124.1583	0.01394284	28.3	32.26	0.58
J103015-270743	759425	157.5651	-27.1287	14.5215	69.0066	215.2906	0.03749136	153.4	35.93	0.58
J103114-295837	722930	157.809	-29.9771	14.6759	59.2068	109.4269	0.01511548	45.7	33.3	0.58
J103139-273049	753808	157.9143	-27.5138	14.3307	51.334	165.215	0.01305822	85.1	34.65	0.58
J103141-300815	720959	157.921	-30.1377	14.8566	62.8353	97.786	0.01849056	40.2	33.02	0.58
J103240-282058	742765	158.169	-28.3495	12.6848	71.4757	181.3984	0.01422809	47.6	33.39	0.58
J103241-273137	31149	158.1721	-27.5271	12.0583	71.4757	147.6499	0.01391053	24.2	31.91	0.58
J103257-250937	782023	158.2381	-25.1609	14.5155	62.1144	243.2447	0.02565921	192.8	36.43	0.62
J103258-274013	31171	158.2426	-27.6711	13.0522	70.8908	126.9981	0.01160875	28.7	32.29	0.58
J103348-271429	757813	158.452	-27.2417	13.1222	56.1694	346.7011	0.03655502	198.6	36.49	0.58
J103353-274945	31238	158.4748	-27.8291	12.2977	60.448	214.9652	0.01032262	54.9	33.7	0.58
J103359-301003	31242	158.4966	-30.1677	9.8673	78.7202	407.8787	0.01277512	60.3	33.9	0.58
J103420-265408	92288	158.5865	-26.9023	14.011	78.9802	135.4984	0.01362264	50.5	33.51	0.58



J103502-293019	728536	158.7604	-29.5062	12.3451	49.8231	111.2483	0.01362627	16.1	31.04	0.58
J103507-275923	31334	158.783	-27.9905	12.1861	73.7025	168.7821	0.00926373	33.0	32.59	0.58
J103521-274137	31355	158.8391	-27.6938	13.2414	75.6965	175.4385	0.01079559	57.7	33.81	0.58
J103547-290131	31390	158.9463	-29.0252	13.0973	50.2235	312.2781	0.03381084	161.0	36.03	0.58
J103609-244856	31415	159.0412	-24.8154	13.0609	53.8966	84.1631	0.00454496	13.2	30.61	0.58
J103645-281010	744989	159.1902	-28.1698	13.2636	49.0161	162.9367	0.01278334	50.7	33.53	0.58
J103646-293253	31484	159.196	-29.5482	13.2256	51.334	197.2334	0.01304613	71.5	34.27	0.58
J103650-270902	31490	159.2096	-27.1485	13.177	67.8558	292.5814	0.03859519	147.7	35.85	0.58
J103651-260227	31491	159.2131	-26.0412	13.526	49.8231	204.1734	0.00907223	87.7	34.72	0.58
J103653-270311	31494	159.2211	-27.0532	12.0485	54.6596	234.1461	0.01299891	57.6	33.8	0.58
J103655-265412	762452	159.233	-26.9029	13.0441	64.2723	199.8074	0.01197818	67.4	34.14	0.58
J103701-284018	738882	159.2551	-28.6725	14.2125	65.4907	236.2912	0.03368768	158.7	36.0	0.58
J103704-252038	31514	159.2683	-25.3441	12.3722	76.8078	199.2584	0.01353874	49.2	33.46	0.58
J103737-261641	31574	159.4074	-26.2776	10.7246	53.0503	322.8375	0.01385994	57.5	33.8	0.58
J103803-281007	31602	159.5132	-28.1688	14.1108	72.5815	304.9854	0.03634067	245.6	36.95	0.58
J103809-260453	31612	159.5414	-26.0815	13.0599	72.73	144.5152	0.0130769	36.8	32.83	0.58
J103818-285307	31626	159.5743	-28.8845	11.4949	74.69	297.56	0.01578427	70.3	34.23	0.58
J103828-283056	740766	159.6196	-28.5157	13.8722	52.6631	169.7936	0.01568042	72.6	34.3	0.58
J103840-283405	31642	159.6679	-28.5684	10.4866	64.4158	323.7424	0.01272478	51.8	33.57	0.58
J103858-300500	3758554	159.7422	-30.084	15.1371	63.8418	81.3298	0.01370769	32.2	32.54	0.6
J103902-291255	31664	159.7607	-29.2144	13.9916	62.6913	165.4385	0.01181481	73.0	34.32	0.58
J103905-265519	93061	159.7724	-26.9228	12.8866	66.2069	350.8164	0.0363276	182.2	36.3	0.58
J103918-265030	31683	159.8261	-26.8421	10.3241	72.1376	344.6117	0.01142924	54.1	33.67	0.58
J103922-293505	31690	159.8422	-29.5846	11.6635	48.8537	274.8887	0.01408946	65.4	34.08	0.58
J104000-292445	31732	160.0014	-29.4123	13.127	66.3502	184.4949	0.01371067	60.3	33.9	0.58
J104004-301606	31738	160.0178	-30.2679	10.59	65.634	286.5209	0.01248467	43.1	33.17	0.58
J104058-274546	750199	160.2427	-27.7623	14.349	67.1384	162.7876	0.01446573	83.4	34.61	0.58
J104059-270456	31805	160.2475	-27.0819	9.6466	56.2443	396.914	0.01698876	51.8	33.57	0.58
J104100-284430	31809	160.2552	-28.7418	12.2681	55.5679	192.7746	0.01365658	44.1	33.22	0.58
J104139-254049		160.4145	-25.6805	14.4528	54.6596	122.5896	0.01404383	51.2	33.54	0.58
J104139-274639	31852	160.4136	-27.778	13.753	59.865	136.4406	0.01569824	45.4	33.28	0.58
J104157-264302		160.4888	-26.7174	13.6008	63.4108	256.0838	0.03786389	139.5	35.72	0.58
J104239-300357		160.6646	-30.0664	15.6547	69.6565	82.1224	0.00940569	41.7	33.1	0.6
J104245-264738	31924	160.6913	-26.7937	12.522	57.7338	345.3264	0.03673843	149.5	35.87	0.58
J104252-252014		160.7192	-25.3373	13.8052	48.935	126.0006	0.02245921	40.0	33.01	0.58
J104311-261500	31951	160.7974	-26.2501	10.1873	61.1016	430.6217	0.01629157	77.5	34.45	0.58
J104326-251857	31960	160.859	-25.316	13.5057	48.6094	125.2967	0.01373015	34.5	32.69	0.58
J104339-285157	31981	160.913	-28.8661	10.9693	76.7273	283.5747	0.01271548	50.4	33.51	0.58
J104414-271548	757564	161.0589	-27.2637	14.1818	59.1335	226.0111	0.03779767	143.8	35.79	0.58
J104442-290119	734399	161.1761	-29.0214	15.2513	59.1335	137.4706	0.03477507	91.8	34.81	0.58
J104524-251723	780619	161.3536	-25.2898	13.9341	50.9391	271.7404	0.04946774	181.9	36.3	0.58
J104620-293733	727073	161.586	-29.626	13.0861	56.9913	269.5008	0.04061149	121.2	35.42	0.58
J104629-253308	32175	161.6229	-25.5523	14.8472	65.7056	145.9224	0.01318261	85.3	34.66	0.59

Table A2: Norma HI data from WALLABY phase 1 pilot survey.

Name	PGC	RA	DEC	$W_{1tot}$	$i$	$W_{mx}$	$z_{cmb}$	$d_L$	$\mu$	$e_\mu$
J163435-620248	58527	248.647418	-62.046778	12.5906	62.8353	234.9112	0.01511102	74.4	34.36	0.58
J163749-621352	4077297	249.454206	-62.231162	10.5802	54.7356	175.1385	0.01625367	16.9	31.14	0.58
J163927-594844	3078607	249.866523	-59.812295	12.0403	67.2818	471.588	0.03785902	216.1	36.67	0.58
J164107-605902	58755	250.281497	-60.983986	13.5023	80.7086	160.1005	0.01186631	54.7	33.69	0.59
J164113-603202		250.307194	-60.534109	13.7705	56.9913	186.0271	0.03986854	82.3	34.58	0.58
J164206-613441	3078658	250.528374	-61.578262	14.1884	71.4757	191.9448	0.01770498	105.9	35.12	0.58
J164249-610527	92488	250.707724	-61.091025	10.6964	79.8702	310.8455	0.01506462	52.8	33.61	0.58
J164355-620233	349886	250.981502	-62.042582	12.6012	52.973	379.5319	0.03933249	185.4	36.34	0.58
J164437-605103	58893	251.156286	-60.851094	10.5273	72.0638	424.6372	0.01781932	88.3	34.73	0.58
J164455-575030	3078727	251.230899	-57.841714	12.282	47.209	400.6343	0.04826815	177.3	36.24	0.58
J164508-611614		251.285273	-61.27071	13.1157	79.3316	171.9725	0.01246623	52.5	33.6	0.58
J164727-575143	3078771	251.863957	-57.862209	13.2117	62.8353	361.9206	0.04771013	224.5	36.76	0.58
J164739-570817	393557	251.914425	-57.138085	14.3561	54.7356	83.2827	0.00287685	23.5	31.86	0.59
J164749-613936		251.954282	-61.660226	12.805	63.5545	174.2319	0.01770366	46.6	33.34	0.58
J164826-623040	343635	252.108723	-62.511225	11.9037	62.8353	185.4562	0.01496239	34.6	32.7	0.58
J164911-620001	350325	252.298069	-62.000386	12.6063	57.7338	275.5516	0.05177993	101.3	35.03	0.58
J165131-603514	59130	252.882699	-60.587289	12.5929	64.9176	133.5985	0.01132893	25.6	32.04	0.58
J165439-605730		253.663341	-60.95855	14.0336	69.2952	168.9091	0.01054331	77.4	34.44	0.58
J165455-610856	357773	253.730344	-61.149002	15.647	54.7356	105.3281	0.01482964	66.5	34.11	0.59
J165520-592615	3078940	253.834941	-59.437529	13.5311	75.2293	153.058	0.01655333	50.9	33.54	0.58
J165559-592439	165948	253.997339	-59.410888	11.7775	47.6238	265.3185	0.01615457	64.4	34.04	0.58
J165632-594959	4584387	254.134589	-59.833236	11.8378	54.5836	468.7337	0.04802051	194.6	36.45	0.58
J165644-622413	4075676	254.184255	-62.403763	9.9351	64.3441	377.1867	0.01719366	53.7	33.65	0.58
J165645-620555		254.191411	-62.098772	15.3289	58.4722	195.9205	0.03011796	186.1	36.35	0.59
J165840-582909	141869	254.669097	-58.485927	11.0622	54.7356	307.411	0.02063727	61.2	33.93	0.58
J165847-612501		254.69821	-61.416959	14.2337	74.4606	160.8808	0.01597719	77.4	34.44	0.59
J165934-623256	4080474	254.894684	-62.548998	10.5454	57.1401	255.9524	0.01642583	34.1	32.66	0.58
J170039-584218	377019	255.16626	-58.705246	13.4896	69.2952	183.8757	0.02094197	70.8	34.25	0.59
J170116-621215	165971	255.317106	-62.204321	12.073	55.039	406.3242	0.04637359	165.4	36.09	0.58
J170149-603901	165952	255.455525	-60.650362	12.2495	65.3475	290.4757	0.01649612	95.0	34.89	0.58
J170232-584322	165953	255.634453	-58.722864	11.5633	60.1568	314.7373	0.02064314	80.6	34.53	0.58
J170349-595038		255.954693	-59.844105	13.0267	49.0161	253.0155	0.01982964	104.6	35.1	1.1
J170700-600654	165955	256.751847	-60.11503	12.2699	62.1144	227.4055	0.01436001	60.3	33.9	0.58
J170747-595059	59659	256.947861	-59.849852	11.7537	79.1552	281.0189	0.01579552	71.0	34.26	0.58
J171120-603454	362143	257.833867	-60.581908	14.2512	50.0636	95.2061	0.01670085	28.9	32.3	0.58
J171134-610802		257.893397	-61.134105	16.0695	54.7356	97.9796	0.00902464	70.5	34.24	0.6
J171309-603124	362690	258.287752	-60.523391	13.4709	70.4539	125.2158	0.01621556	33.9	32.65	0.58
J171339-615822	92494	258.415875	-61.973005	15.4747	64.2723	152.0756	0.01505209	123.2	35.45	0.59
J171538-602409		258.909689	-60.402582	13.0023	79.9614	243.7314	0.0195147	96.4	34.92	0.58
J171558-590923		258.994367	-59.156581	13.0923	72.0638	189.1948	0.01186545	62.2	33.97	0.58
J171850-601104	365445	259.711772	-60.184587	13.7175	47.1257	253.8042	0.01551251	144.7	35.8	0.58
J171924-615016	92496	259.853206	-61.837997	13.265	75.2293	276.1248	0.02455815	137.8	35.7	0.58

Table A3: Eridanus HI data from WALLABY phase 1 pilot survey.

Name	PGC	RA	DEC	$W_{1tot}$	$i$	$W_{mx}$	$z_{cmb}$	$d_L$	$\mu$	$e_\mu$
J034114-235017	13561	55.308333	-23.838056	10.1562	51.4127	254.5868	0.00591068	28.2	32.25	0.58
J033859-223502	13442	54.745833	-22.583889	13.3234	62.5472	171.2887	0.01408583	57.3	33.79	0.58
J034056-223350	13544	55.233333	-22.563889	8.0092	64.7743	374.7365	0.00478841	21.8	31.7	0.58
J034517-230001	13760	56.320833	-23.000278	9.306	56.1694	361.1469	0.00483078	37.0	32.84	0.58
J034219-224520	13608	55.579167	-22.755556	11.9271	51.6485	145.3675	0.00485579	22.1	31.72	0.58
J033941-235054	13477	54.920833	-23.848333	13.8833	82.0066	71.6966	0.00503014	14.2	30.77	0.58
J034057-214245	13543	55.2375	-21.7125	11.5644	74.9975	148.0462	0.00527728	19.3	31.43	0.58
J034040-221711	13531	55.166667	-22.286389	12.4245	77.6238	154.5925	0.00553255	31.2	32.47	0.58
J034002-192200	13491	55.008333	-19.366667	12.0881	80.6134	114.5336	0.00365656	15.1	30.9	0.58
J034814-212824	13871	57.058333	-21.473333	9.6576	55.1904	274.0381	0.00493632	25.8	32.06	0.58
J034337-211418	13689	55.904167	-21.238333	12.4218	72.5815	128.9114	0.00499355	22.1	31.72	0.58
J034434-211123	135119	56.141667	-21.189722	13.1936	70.0185	72.3556	0.00488434	10.6	30.12	0.58
J034131-214051	13569	55.379167	-21.680833	10.3246	74.4606	157.7669	0.00506959	12.3	30.45	0.58
J033921-212450	13460	54.8375	-21.413889	11.9631	66.4218	117.8377	0.00503156	15.1	30.89	0.58
J033537-211742	13283	53.904167	-21.295	11.8244	75.2293	146.8529	0.00562052	21.5	31.66	0.58
J033341-212844	13184	53.420833	-21.478889	8.9854	48.6094	265.2557	0.00578946	17.8	31.25	0.58
J033347-192946	13190	53.445833	-19.496111	10.187	54.7356	231.4768	0.00615231	23.9	31.89	0.58
J033810-194412	13401	54.541667	-19.736667	12.6368	71.7693	175.8256	0.01352603	43.9	33.21	0.58
J033757-213938	13392	54.4875	-21.660556	13.5581	73.552	136.5896	0.01347565	41.6	33.09	0.58
J033147-211309	831121	52.945833	-21.219167	14.354	64.9892	101.5197	0.01371815	34.2	32.67	0.58
J032455-214701	12762	51.229167	-21.783611	12.8097	55.1904	102.3076	0.00439474	17.0	31.16	0.58
J032425-213233	12737	51.104167	-21.5425	8.4969	72.5815	341.6675	0.00484116	23.0	31.8	0.58
J033527-211302	831168	53.8625	-21.217222	12.8515	48.4461	120.2676	0.00466241	23.6	31.86	0.58
J032735-211339	12889	51.895833	-21.2275	11.3398	75.7749	166.0928	0.00517694	21.7	31.68	0.58
J032831-222957	813307	52.129167	-22.499167	13.6391	73.7025	69.8049	0.00548873	12.1	30.41	0.58
J033653-245445	13342	54.220833	-24.9125	12.2326	58.3248	124.5537	0.00575066	19.0	31.39	0.58
J033302-240756	13154	53.258333	-24.132222	12.6236	71.4757	162.4149	0.00598226	37.5	32.87	0.58
J033617-253615	13304	54.070833	-25.604167	11.4992	67.3535	124.6075	0.00493199	13.5	30.66	0.58
J032937-232103	12986	52.404167	-23.350833	12.9769	74.3844	116.2925	0.00509535	23.5	31.85	0.58
J033326-234246	13171	53.358333	-23.712778	9.5617	76.0108	256.6107	0.00564806	21.8	31.69	0.58
J033228-232245	13127	53.116667	-23.379167	13.3847	56.3192	69.6998	0.00543831	10.7	30.15	0.58



---

J124350-003344	42847	190.96079	-0.56243	9.5363	48.4461	265.9249	0.00990722	23.0	31.81	0.58
J124421+042536	42892	191.08944	4.42672	12.0215	60.6661	303.9758	0.02972201	93.2	34.85	0.58
J124428-030017	42909	191.11791	-3.0048	11.1596	49.7428	453.3832	0.02503503	133.7	35.63	0.58
J124428+002815	42910	191.119	0.47091	10.9498	79.3316	103.7941	0.00506443	7.4	29.36	0.58
J124433-021916	42921	191.14097	-2.32119	12.8803	55.1904	133.9742	0.00643985	29.3	32.34	0.58
J124508-002747	42975	191.28452	-0.46322	6.6948	66.1353	422.087	0.00619415	14.9	30.87	0.58
J124531-003203	3110155	191.38242	-0.53434	10.5016	58.0296	157.9589	0.00652746	13.4	30.64	0.58
J124548-002600	1143451	191.45039	-0.43347	13.7782	53.6665	74.4803	0.00670022	14.6	30.82	0.58
J124608+042643	1268285	191.53441	4.4453	13.9988	65.8488	229.0488	0.02473573	135.6	35.66	0.58
J124645+055723	43106	191.69058	5.95643	10.8463	55.9442	143.6344	0.0038936	13.1	30.59	0.58
J124651-013308	3295908	191.71291	-1.55242	14.837	56.7677	69.3402	0.02402866	20.8	31.59	0.59
J124701-013444	43128	191.75426	-1.57889	12.1334	49.8231	198.9382	0.01021996	44.0	33.22	0.58
J124717+002405	43153	191.82103	0.40156	11.0785	60.6661	156.0027	0.04758206	17.1	31.16	0.58
J124753-011107	43198	191.97243	-1.18529	11.8646	69.8012	349.4939	0.02458987	113.0	35.26	0.58
J124800+042609	3994854	192.0002	4.43583	12.4899	56.2443	155.1573	0.00450877	32.4	32.55	0.58
J125038+012749	43470	192.66139	1.46365	10.874	79.7794	175.7894	0.00535511	19.5	31.45	0.58
J124808+033759	5808028	192.03338	3.63328	14.7059	54.7356	93.0806	0.02466785	34.1	32.67	0.7

---

This paper has been typeset from a  $\text{\TeX}/\text{\LaTeX}$  file prepared by the author.